HHS Public Access

Author manuscript

Magn Reson Med. Author manuscript; available in PMC 2023 July 01.

Published in final edited form as:

Magn Reson Med. 2022 August ; 88(2): 691–710. doi:10.1002/mrm.29232.

MaxGIRF: Image Reconstruction Incorporating Concomitant Field and Gradient Impulse Response Function Effects

Nam G. Lee[1],

Rajiv Ramasawmy[2],

Yongwan Lim[3],

Adrienne E. Campbell-Washburn[2],

Krishna S. Nayak[1,3]

[1]Department of Biomedical Engineering, University of Southern California, Los Angeles, California, USA

[2]Cardiovascular Branch, Division of Intramural Research, National Heart, Lung, and Blood Institute, National Institutes of Health, Bethesda, Maryland, USA

[3]Ming Hsieh Department of Electrical and Computer Engineering, University of Southern California, Los Angeles, California, USA

Abstract

Purpose: To develop and evaluate an improved strategy for compensating concomitant field effects in non-Cartesian MRI at the time of image reconstruction.

Theory: We present a higher-order reconstruction method, denoted MaxGIRF, for non-Cartesian imaging that simultaneously corrects off-resonance, concomitant fields, and trajectory errors without requiring specialized hardware. Gradient impulse response functions are used to predict actual gradient waveforms, which are in turn used to estimate the spatiotemporally varying concomitant fields based on analytic expressions. The result, in combination with a reference field-map, is an encoding matrix that incorporates a correction for all three effects.

Methods: MaxGIRF reconstruction is applied to noiseless phantom simulations, spiral gradient echo imaging of an ISMRM/NIST phantom, axial and sagittal multi-slice spiral spin-echo imaging of a healthy volunteer at 0.55T. MaxGIRF was compared against previously established concomitant field compensation and image correction methods. Reconstructed images are evaluated qualitatively and quantitatively using normalized root mean square error. Finally, a low-rank approximation of MaxGIRF is employed to reduce computational burden. The accuracy of the low-rank approximation is studied as a function of minimum rank.

Results: MaxGIRF reconstruction successfully mitigated blurring artifacts both in phantoms and in vivo and was effective in regions where concomitant fields counteract static off-resonance,

Correspondence to: Nam G. Lee, MS, 3740 McClintock Ave, EEB 414, University of Southern California, Los Angeles, CA, 90089-2564, Phone: (213) 471-5668, namgyunl@usc.edu.
A.C.W. and K.S.N. should be considered joint senior author.

A preliminary version of this work was presented at ISMRM 2021, Abstract #624.

superior to the comparator method. A minimum rank of 8 and 30 for axial and sagittal scans, respectively, gave less than 2% error compared with the full-rank reconstruction.

Conclusion: MaxGIRF reconstruction simultaneously corrects off-resonance, trajectory errors, and concomitant field effects. The impact of this method is greatest when imaging with longer readouts and/or at lower field strength.

Keywords

MRI reconstruction; gradient distortion; concomitant fields; gradient impulse response function; expanded signal model

INTRODUCTION

Image quality from magnetic resonance imaging (**MRI**) that utilizes non-Cartesian sampling, particularly spirals, has improved continuously over the past 30 years. Current state-of-the-art spiral MRI provides quality that is comparable to its 2D/3D Cartesian counterparts, and is appropriate for clinical use (1,2). Spiral acquisitions are attractive because they provide high scan and SNR efficiency, robustness to motion artifacts, and are advantageous for fast imaging applications such as MR fingerprinting (3,4) and cardiac imaging (5).

Spiral imaging requires overcoming unique challenges, notably off-resonance, gradient distortion, and concomitant field effects. The first two effects are well known in the literature; static off-resonance leads to local blurring and gradient distortion results in trajectory errors that manifest themselves as halo artifacts near edges. The effects of concomitant fields are less widely recognized, but are extremely important for long readouts, scan planes farther from isocenter, and at low B0 field strengths. Concomitant fields constitute an additional nonrotating magnetic field (B_x, B_y) in the laboratory reference frame whenever linear gradients are active (6). Spatial encoding in MRI is achieved by the Larmor frequency, which is proportional to the magnitude of the applied magnetic field. The applied magnetic field is a superposition of the homogeneous (B_o) main magnetic field and the transverse ($B_x(t)$, $B_y(t)$) field and longitudinal field ($B_z(t)$) produced by a gradient coil. The dot product of three gradient fields $\mathbf{G}(t) = \left(\frac{dB_z(t)}{dx}, \frac{dB_z(t)}{dy}, \frac{dB_z(t)}{dz}\right)^T$ with a spatial position causes a linear frequency offset. In contrast, the transverse component contributes a nonlinear, higher-order frequency offset, which is represented as a sum of products of quadratic gradients with higher-order spatial terms (e.g., $G_{y,i}(t)G_{z,i}(t)xz$). Therefore, spiral imaging accrues a spatiotemporally varying phase due to concomitant fields in addition to static off-resonance (7).

Several previous works successfully mitigate concomitant field effects by means of image reconstruction method (7–9). King et al. (7) proposed a concomitant field correction method based on frequency-segmented deblurring, referred to here as King's method. This approach uses approximations to separate the concomitant field phase into a time-dependent parameter consisting of the time integral of common gradient terms and the rest as a time-independent frequency offset. King's method then performs frequency-segmented

deblurring. Two recent approaches by Chen et al. (8) and Cheng et al. (10) achieve a more computationally efficient reconstruction and simultaneously correct static off-resonance and concomitant fields based on King's approximations.

Wilm et al. (11) proposed a powerful general approach using NMR field probes (12,13) in conjunction with a higher-order encoding model, which inspires this work. This approach incorporates higher-order dynamic fields to the encoding process and has demonstrated excellent image quality for several applications, including diffusion (11,14) and structural imaging (15). A dynamic field camera (16,17) consisting of spatially distributed NMR field probes is used to measure phase evolutions at various positions for high-order field expansions with globally smooth functions (11,14,18). The NMR field probes provide real-time monitoring of field evolutions from various sources, however commercially available systems are fairly expensive and building an in-house system from scratch requires expertise beyond most MRI labs (12,17,19–21). Therefore, although very promising, the higher-order approach relying on field-camera measurements is not widely available.

The characterization of gradient distortions with gradient impulse response functions (**GIRFs**) (22,23) can be a reasonable surrogate for NMR field probes. Assuming a linear time invariant (**LTI**) system model for the gradient chain, GIRFs capture gradient delays, eddy current effects, and mechanically induced field oscillations. For each gradient axis, an MR system is perturbed with a set of input gradients and field responses are measured with either a dynamic field camera or phantom-based methods. Field-camera measurements provide both self-responses and cross-responses (e.g., input gradient on the x-axis and field response on the y-axis) in a single measurement, thereby allows the full characterization of a multiple-input, multiple-output LTI system (23,24). On the other hand, phantom-based methods typically measure only self-term GIRFs (25) and B_0 cross-terms (26). Phantom-based GIRFs have proven to be effective in several applications, including RF pulse design (27,28), eddy current-induced artifact correction (29), and image reconstruction (30–32). Therefore, the phantom-based method appears to be a reasonable compromise to an accurate, albeit expensive field monitoring device.

In this work, because concomitant fields are analytically expressed with gradients and spatial coordinates, we hypothesize that gradients predicted with phantom-based GIRFs can better estimate concomitant fields than nominal gradients. Following this, we propose a novel higher-order image reconstruction method, denoted **MaxGIRF**, that incorporates concomitant fields, static off-resonance, and GIRF trajectory corrections. The "Max" part of the MaxGIRF acronym reflects the fact that the concomitant fields are also known as "Maxwell fields" in the literature because they are based on the principles of electromagnetism described by Maxwell's equations. This proposed framework can be considered as a surrogate to NMR field probes that requires no special hardware but requires a good analytic model of concomitant fields that depends on coil geometry (6,33) and severity of gradient nonlinearity (34). Non-Cartesian imaging with long readouts generally benefits from this method, but its impact will be greatest at high-performance low-field systems (35,36) because the effect of concomitant fields scales quadratically with the maximum gradient amplitude and inversely to the main magnetic field B_0.

We first validate the proposed method using noiseless simulations at various field strengths and off-center positions. A guideline for selecting an optimal rank is provided when a low-rank approximation is applied to the MaxGIRF encoding model. MaxGIRF reconstructions using nominal and GIRF-predicted gradients are compared at 0.55T using an ISMRM/NIST system phantom. Finally, MaxGIRF reconstructions are demonstrated in vivo using axial and sagittal spiral spin-echo data of the head and neck, and made available open source.

THEORY

In this work, we address sequences where the net phase of all isochromats within a voxel prior to the next RF pulse can be ignored, e.g., any pulse sequences with spoiler gradients at the end of each TR.

2.1 MaxGIRF encoding

Figure 1 illustrates the overall steps to calculate MaxGIRF encoding matrices. Let $\mathbf{G}_{\mathrm{L}}(t)$ and $\mathbf{G}_{\mathrm{P}}(t)$ be the gradients in the logical coordinate system and physical coordinate system, respectively. Unless clearly specified, we use the physical coordinate system exclusively and describe variables without the subscript for clarity, e.g., $\mathbf{G}(t) = \mathbf{G}_{\mathrm{P}}(t)$. Using a modified version of the expanded signal model (11,24,37), the measured **k**-space data over the region of interest V is expressed as:

$$d_{i,c}(t) = \int_V m(\mathbf{r}) S_c(\mathbf{r}) \exp(-j\phi_i(\mathbf{r},t)) d\mathbf{r} + n_{i,c}(t) \quad [1]$$

where $d_{i,c}$ denotes the i-th interleaf, c-th receive coil **k**-space data of the target image $m(\mathbf{r})$, $S_c(\mathbf{r})$ the receive coil sensitivity at position **r** of the c-th coil, $\phi_i(\mathbf{r}, t)$ the time-varying phase of a voxel at position **r** in radians, and $n_{i,c}$ the measurement noise. The indices i and c count the N_i interleaves and N_c receive coils, respectively. The MaxGIRF approach models the magnitude of the spatiotemporal magnetic field $\|\mathbf{B}_i(\mathbf{r},t)\|_{\ell_2}$ as a sum of gradients $\mathbf{G}_i(t) = \left[G_{\mathrm{x},i}(t), G_{\mathrm{y},i}(t), G_{\mathrm{z},i}(t)\right]^T$ in millitesla per meter, static off-resonance $\Delta f(\mathbf{r})$ in hertz, and concomitant fields in tesla (6):

$$\|\mathbf{B}_i(\mathbf{r},t)\|_{\ell_2} = B_0 + \mathbf{G}_i(t)\cdot\mathbf{r} + 2\pi\Delta f(\mathbf{r})/\gamma + \sum_{\ell=4}^{N_\ell} h_{\ell,i}(t) p_\ell(\mathbf{r}), \quad [2]$$

where ℓ counts the N_ℓ concomitant field terms, p_ℓ is the ℓth concomitant field basis function (in m^2 or m^3) and $h_{\ell,i}$ is the ℓth dynamic coefficient (in T/m^2 or T/m^3), expressed as a function of the i-th gradient waveforms, and γ is the gyromagnetic ratio (in rad/sec/T). Analytic expressions of $\{h_{\ell,i}(t)\}_{\ell=1}^{N_\ell}$ and $\{p_\ell(\mathbf{r})\}_{\ell=1}^{N_\ell}$ for a symmetric gradient system used in this study (6) are given in Table 1. The linear gradients are described as the first three terms in the concomitant field basis functions. Note that linear gradients $G_i(t)$ can be either GIRF-predicted gradients $\mathbf{G}_i^{\mathrm{pred}}(t)$ or nominal gradients $\mathbf{G}_i^{\mathrm{nom}}(t)$. Time integration of the magnetic field (after the demodulation of its carrier frequency) multiplied by the

gyromagnetic ratio γ, $\gamma\int_0^t \|\mathbf{B}_i(\mathbf{r},\tau)\|_{\ell_2} d\tau$, then gives the phase evolution of a voxel at position $\mathbf{r}$ as:

$$\begin{aligned}\phi_i(\mathbf{r},t) &= \mathbf{k}_i(t)\cdot\mathbf{r} + 2\pi\Delta f(\mathbf{r})t + \sum_{\ell=4}^{N_\ell} k_{\ell,i}(t)p_\ell(\mathbf{r}),\\ &= \mathbf{k}_i(t)\cdot\mathbf{r} + \widetilde{\phi}_i(\mathbf{r},t),\end{aligned} \quad [3]$$

where $k_{\ell,i}(t)$ is the ℓth phase coefficient obtained by $k_{\ell,i}(t) = \gamma\int_0^t h_{\ell,i}(\tau)d\tau$, and $\widetilde{\phi}_i(\mathbf{r},t)$ denotes a phase term consisting of static off-resonance and concomitant fields. Note that the reference time point starts at the isodelay of an RF pulse for GRE pulse sequences and the echo time (**TE**) for spin-echo pulse sequences when spiral readouts start at TE. Let N_k denote the number of **k**-space samples per interleaf. Let $\mathbf{R}_{\mathrm{LtoP}}$ be a 3 × 3 orthogonal transformation matrix from the logical coordinate system to the physical coordinate system. Note that $(\mathbf{R}_{\mathrm{LtoP}})^{\mathbf{T}} = (\mathbf{R}_{\mathrm{LtoP}})^{-1} = \mathbf{R}_{\mathrm{PtoL}}$. Then we have

$$\mathbf{k}_{P,i}(t) = \mathbf{R}_{LtoP}\mathbf{k}_{L,i}(t) \quad [4a]$$

$$\mathbf{r}_{\mathrm{P}} = \mathbf{R}_{\mathrm{LtoP}}\mathbf{r}_{\mathrm{L}} + \mathbf{r}_{\mathrm{P,offset}} \quad [4b]$$

where $\mathbf{r}_{\mathrm{P,offset}}$ represents the offset of a scan plane from isocenter in the physical coordinate system. With Equations 4a and 4b, we can express the k-space phase $\mathbf{k}_i(t)\cdot\mathbf{r}$ in terms of variables in the logical coordinate system:

$$\begin{aligned}\mathbf{k}_{\mathrm{P},i}(t)\cdot\mathbf{r}_{\mathrm{P}} &= \mathbf{k}_{\mathrm{P},i}(t)\cdot\left(\mathbf{R}_{\mathrm{LtoP}}\mathbf{r}_{\mathrm{L}} + \mathbf{r}_{\mathrm{P,offset}}\right)\\ &= \left(\mathbf{R}_{\mathrm{LtoP}}\mathbf{k}_{\mathrm{L},i}(t)\right)^{\mathbf{T}}\mathbf{R}_{\mathrm{LtoP}}\mathbf{r}_{\mathrm{L}} + \mathbf{k}_{\mathrm{P},i}(t)\cdot\mathbf{r}_{\mathrm{P,offset}}\\ &= \mathbf{k}_{L,i}(t)\cdot\mathbf{r}_L + \mathbf{k}_{P,i}(t)\cdot\mathbf{r}_{P,\mathbf{offset}}\end{aligned} \quad [5]$$

The received signal can be expressed using variables both in the logical and physical coordinate systems:

$$\begin{aligned}d_{i,c}(t) &= \int_V m(\mathbf{r})S_c(\mathbf{r})\exp\left(-j\mathbf{k}_{\mathrm{P},i}(t)\cdot\mathbf{r}_{\mathrm{P}}\right)\exp\left(-j\widetilde{\phi}_i(\mathbf{r}_{\mathrm{P}},t)\right)d\mathbf{r} + n_{i,c}(t)\\ &= \exp\left(-j\mathbf{k}_{\mathrm{P},i}(t)\cdot\mathbf{r}_{\mathrm{P,offset}}\right)\times\cdots\\ &\quad\int_V m(\mathbf{r})S_c(\mathbf{r})\exp\left(-j\mathbf{k}_{L,i}(t)\cdot\mathbf{r}_L\right)\exp\left(-j\widetilde{\phi}_i(\mathbf{r}_P,t)\right)d\mathbf{r} + n_{i,c}(t)\end{aligned} \quad [6]$$

Equation 6 indicates that measured **k**-space data is modulated by a time-varying phase term due to a slice offset. If this time-varying phase term is not compensated during data acquisition (38), then the received signal must be demodulated first before further processing because concomitant field correction would not be accurate when voxels are displaced from their true locations. Note that a Fourier matrix is computed with the gradients in the logical coordinate system as done in conventional FFT/NUFFT and a higher-order encoding matrix

is computed with **k**-space trajectories and spatial coordinates in the physical coordinate system. See Supporting Information Text S1 for details about coordinate transformations.

Suppose that an underlying object can be represented as a weighted sum of N ideal voxel shapes defined on an $N_1 \times N_2$ Cartesian grid, i.e., $m(\mathbf{r}) = \sum_{\rho=1}^{N} m(\mathbf{r}_\rho)\delta(\mathbf{r}-\mathbf{r}_\rho)$. Inserting this representation into Equation 1 and discretizing in time leads to

$$\mathbf{d}_{i,c} = \mathbf{E}_i \mathbf{S}_c \mathbf{m} + \mathbf{n}_{i,c}, \quad [7]$$

where $\mathbf{d}_{i,c} = \left[d_{i,c}(t_1), \ldots, d_{i,c}\left(t_{N_k}\right)\right]^T \in \mathbb{C}^{N_k}$ contains the i-th interleaf, c-th coil (demodulated) **k**-space data, $\mathbf{E}_i \in \mathbb{C}^{N_k \times N}$ denotes the i-th encoding matrix, $\mathbf{S}_c \in \mathbb{C}^{N \times N}$ is a diagonal matrix containing the receive coil sensitivities of the c-th coil, $\mathbf{m} = [m(\mathbf{r}_1), \ldots, m(\mathbf{r}_N)]^T \in \mathbb{C}^N$ is a vector of complex image values, and $\mathbf{n}_{i,c} = \left[n_{i,c}(t_1), \ldots, n_{i,c}\left(t_{N_k}\right)\right]^T \in \mathbb{C}^{N_k}$ contains the i-th interleaf, c-th coil measurement noise. The i-th encoding matrix $\mathbf{E}_i$ is expressed as the Hadamard product (element-wise multiplication, denoted $\odot$) of a Fourier matrix $\mathbf{F}_i \in \mathbb{C}^{N_k \times N}$ containing only linear phase terms and a higher-order encoding matrix $\mathbf{H}_i \in \mathbb{C}^{N_k \times N}$ containing other remaining phase terms:

$$\mathbf{E}_i = \mathbf{F}_i \odot \mathbf{H}_i, \quad [8]$$

Where

$$\mathbf{F}_i = \begin{bmatrix} \exp\left(-j\mathbf{k}_{\mathrm{L},i}(t_1)\cdot\mathbf{r}_{\mathrm{L},1}\right) & \cdots & \exp\left(-j\mathbf{k}_{\mathrm{L},i}(t_1)\cdot\mathbf{r}_{\mathrm{L},N}\right) \\ \vdots & \ddots & \vdots \\ \exp\left(-j\mathbf{k}_{\mathrm{L},i}\left(t_{N_k}\right)\cdot\mathbf{r}_{\mathrm{L},1}\right) & \cdots & \exp\left(-j\mathbf{k}_{\mathrm{L},i}\left(t_{N_k}\right)\cdot\mathbf{r}_{\mathrm{L},N}\right) \end{bmatrix}, \quad [9]$$

and

$$\mathbf{H}_i = \begin{bmatrix} \exp\left(-j\tilde{\phi}_i(\mathbf{r}_{\mathrm{P},1}, t_1)\right) & \cdots & \exp\left(-j\tilde{\phi}_i(\mathbf{r}_{\mathrm{P},N}, t_1)\right) \\ \vdots & \ddots & \vdots \\ \exp\left(-j\tilde{\phi}_i\left(\mathbf{r}_{\mathrm{P},1}, t_{N_k}\right)\right) & \cdots & \exp\left(-j\tilde{\phi}_i\left(\mathbf{r}_{\mathrm{P},N}, t_{N_k}\right)\right) \end{bmatrix}. \quad [10]$$

It is important to note that the forward signal model in Equation 1 is described with the forward Fourier transform as commonly done in standard textbooks, but the choice of FFT versus IFFT for transforming k-space data to an image is vendor-specific, and critical for a successful implementation (7,39).

2.2 Image reconstruction

Image reconstruction for MaxGIRF encoding can be formulated as a linear least-squares problem similar to (11,14,37). Specifically, the MaxGIRF approach employs a multi-shot extension of (11):

$$\widehat{\mathbf{m}} = \underset{\mathbf{m}}{\operatorname{argmin}} \sum_{i=1}^{N_i} \sum_{c=1}^{N_c} \|\boldsymbol{d}_{i,c} - \mathbf{E}_i \mathbf{S}_c \mathbf{m}\|_{\ell 2}^2 . \quad [11]$$

Equation 11 often needs to be expressed in the form of $A(\mathbf{m}) = \mathbf{b}$ to be solved with iterative algorithms (e.g., LSQR (40)). Such a form is obtained by taking the derivative of a cost function with respect to $\mathbf{m}$ and setting it equal to zero:

$$\sum_{i=1}^{N_i} \sum_{c=1}^{N_c} \left(A_{i,c}^H A_{i,c}\right)\mathbf{m} = \sum_{i=1}^{N_i} \sum_{c=1}^{N_c} A_{i,c}^H(\mathbf{d}_{i,c}), \quad [12]$$

where $A_{i,c}(\mathbf{x}) = \mathbf{E}_i \mathbf{S}_c \mathbf{x}: \mathbb{C}^N \rightarrow \mathbb{C}^{N_k}$ denotes the linear forward operator that maps a length-N vector of image values to a length-N_k vector of $\mathbf{k}$-space samples of the i-th interleaf and c-th coil, and $A_{i,c}^H(\mathbf{y}) = \mathbf{S}_c^H \mathbf{E}_i^H \mathbf{y}: \mathbb{C}^{N_k} \rightarrow \mathbb{C}^N$ denotes its adjoint. The superscript $(\cdot)^H$ denotes the transposed complex conjugate.

2.3 Low-rank approximation to higher-order encoding matrices

To reduce the computational burden of explicit matrix-vector multiplications and reduce memory requirements, we introduce a low-rank approximation to higher-order encoding matrices following previous approaches (41,42). Suppose the singular value decomposition (**SVD**) of the i-th higher-order encoding matrix $\mathbf{H}_i \in \mathbb{C}^{N_k \times N}$ is given by

$$\mathbf{H}_i = \sum_{\ell=1}^{L_{\max}} \mathbf{u}_{\ell,i} \sigma_{\ell,i} \tilde{\mathbf{v}}_{\ell,i}^H = \sum_{\ell=1}^{L_{\max}} \mathbf{u}_{\ell,i} \mathbf{v}_{\ell,i}^H, \quad [13]$$

where $\mathbf{u}_{\ell,i} \in \mathbb{C}^{N_k}$ denotes the ℓth left singular vector, $\sigma_{\ell,i} \in \mathbb{R}$ the ℓth singular value, $\tilde{\mathbf{v}}_{\ell,i} \in \mathbb{C}^N$ the ℓth right singular vector, and $L_{\max}$ is the true rank of the higher-order encoding matrix $\mathbf{H}_i$. A singular value and the corresponding right singular vector can be combined to yield $\mathbf{v}_{\ell,i} \in \mathbb{C}^N$. The vectors $\mathbf{u}_{\ell,i} \in \mathbb{C}^{N_k}$ and $\mathbf{v}_{\ell,i} \in \mathbb{C}^N$ are hereafter referred to as temporal and spatial basis vectors for the i-th higher-order encoding matrix $\mathbf{H}_i$, respectively. Note that the relation in Equation 13 is exact (no loss in accuracy) and $L_{\max}$ is large (>50) in general. According to the Eckart-Young theorem (43), the rank-L SVD truncation $\widetilde{\mathbf{H}}_i = \sum_{\ell=1}^{L} \mathbf{u}_{\ell,i} \mathbf{v}_{\ell,i}^H$ provides the best rank-L approximation to $\mathbf{H}_i$ in a least-squares sense:

$$\left\|\mathbf{H}_i - \widetilde{\mathbf{H}}_i\right\|_{\mathbf{F}} = \underset{\operatorname{rank}(\mathbf{B}) \leq L}{\operatorname{argmin}} \|\mathbf{H}_i - \mathbf{B}\|_{\mathrm{F}} = \sqrt{\sigma_{L+1}^2 + \cdots + \sigma_{L_{\max}}^2} . \quad [14]$$

We select only one L and apply it to all higher-order encoding matrices. Substituting $\widetilde{\mathbf{H}}_i = \sum_{\ell=1}^{L} \mathbf{u}_{\ell,i} \mathbf{v}_{\ell,i}^H$ into Equation 8 yields

$$\begin{aligned}\mathbf{E}_i &\approx \mathbf{F}_i \odot \left(\sum_{\ell=1}^{L} \mathbf{u}_{\ell,i} \mathbf{v}_{\ell,i}^H \right) \\ &\approx \sum_{\ell=1}^{L} \mathbf{F}_i \odot \left(\mathbf{u}_{\ell,i} \mathbf{v}_{\ell,i}^H \right) \\ &\approx \sum_{\ell=1}^{L} \mathrm{diag}(\mathbf{u}_{\ell,i}) \mathbf{F}_i \mathrm{diag}\left(\mathbf{v}_{\ell,i}^*\right),\end{aligned} \quad [15]$$

where $\mathrm{diag}(\mathbf{u}_{\ell,i}) \in \mathbb{C}^{N_k \times N_k}$ and $\mathrm{diag}\left(\mathbf{v}_{\ell,i}^*\right) \in \mathbb{C}^{N \times N}$ are diagonal matrices containing the elements of the vectors $\mathbf{u}_{\ell i}$ and $\mathbf{v}_{\ell,i}^*$ (the complex conjugate of $\mathbf{v}_{\ell i}$ in the main diagonal, respectively. The last expression is obtained using the special property of the Hadamard product of a dense matrix $\mathbf{F}_i$ with a rank-1 matrix $\mathbf{u}_{\ell,i}\mathbf{v}_{\ell,i}^H$. Using Equation 15, the forward and adjoint operators can be expressed as:

$$A_{i,c}(\mathbf{x}) = \mathbf{E}_i \mathbf{S}_c \mathbf{x} \approx \sum_{\ell=1}^{L} \mathrm{diag}(\mathbf{u}_{\ell,i}) \mathbf{F}_i \mathrm{diag}\left(\mathbf{v}_{\ell,i}^*\right) \mathbf{S}_c \mathbf{x}, \quad [16a]$$

$$A_{i,c}^H(\mathbf{y}) = \mathbf{S}_c^H \mathbf{E}_i^H \mathbf{y} \approx \mathbf{S}_c^H \sum_{\ell=1}^{L} \mathrm{diag}(\mathbf{v}_{\ell,i}) \mathbf{F}_i^H \mathrm{diag}\left(\mathbf{u}_{\ell,i}^*\right) \mathbf{y}\,. \quad [16b]$$

Equation 16 indicates that an expensive, explicit matrix-vector multiplication with an encoding matrix $\mathbf{E}_i$ (and $\mathbf{E}_i^H$) can be replaced by L summations of a fast routine for $\mathbf{F}_i$ such as FFT followed by inverse gridding (44) or non-uniform fast Fourier transforms (**NUFFT**) (45).

2.4 Static off-resonance map estimation

MaxGIRF reconstruction requires an accurate and spatially smooth static off-resonance map. For this purpose, we acquire a series of Cartesian GRE datasets at different echo times. Since the MaxGIRF encoding model does not separate water/fat components, we consider the image content $\rho = [\rho(\mathbf{r}_1), \ldots, \rho(\mathbf{r}_N)]^T \in \mathbb{C}^N$ as a sum of water/fat, and model static off-resonance $\Delta\mathbf{f} = [\Delta f(\mathbf{r}_1), \ldots, \Delta f(\mathbf{r}_N)]^T \in \mathbb{R}^N$ (in Hz) as a sum of $\mathbf{E}_0$ inhomogeneity and the water/fat chemical shift (e.g., −3.8 ppm, −88 Hz at 0.55T). We perform image-based parameter estimation using nonlinear inversion optimization (**NLINV**), inspired by a recent work on water/fat separation and B_0 inhomogeneity mapping (46,47). Specifically, the forward signal model is defined as:

$$\mathbf{F}_m(\mathbf{x}) = \boldsymbol{\rho} \odot \exp(j2\pi\Delta\mathbf{f}\mathrm{TE}_m) = \begin{bmatrix} \rho(\mathbf{r}_1) \\ \vdots \\ \rho(\mathbf{r}_N) \end{bmatrix} \odot \begin{bmatrix} \exp(j2\pi\Delta f(\mathbf{r}_1)\mathrm{TE}_m) \\ \vdots \\ \exp(j2\pi\Delta f(\mathbf{r}_N)\mathrm{TE}_m) \end{bmatrix} \quad [17]$$
$$= \mathrm{diag}(\exp(j2\pi\Delta\mathbf{f}\mathrm{TE}_m))\boldsymbol{\rho} = \mathrm{diag}(\boldsymbol{\rho})\exp(j2\pi\Delta\mathbf{f}\mathrm{TE}_m)$$
$$\text{with unknown } \mathbf{x} = \left[\boldsymbol{\rho}^T, \Delta\mathbf{f}^T\right]^T \text{ and } m = 1, \ldots N_e,$$

where $\mathbf{F}_m(\mathbf{x}) \in \mathbb{C}^N$ is a length-N vector of the estimated m-th echo-time image, N_e denotes the number of echo times, TE_m is the m-th echo time in sec, and the symbol $\odot$ denotes the Hadamard product. Equation 17 is solved with the a slight modification of the iteratively regularized Gauss-Newton method (**IRGNM**) as described by (46). The modified cost function is given as:

$$\Phi(\hat{\mathbf{x}}) = \underset{\hat{\mathbf{x}}}{\mathrm{argmin}} \|\mathbf{y} - \mathbf{G}(\hat{\mathbf{x}})\|_{\ell_2}^2 + \alpha\|\hat{\mathbf{x}} - \hat{\mathbf{x}}_0\|_{\ell_2}^2 \text{with } \mathbf{x} = \mathbf{W}\hat{\mathbf{x}} \text{ and } \mathbf{G}(\hat{\mathbf{x}}) = \mathbf{F}(\mathbf{W}\hat{\mathbf{x}}), \quad [18]$$

where $\mathbf{y} \in \mathbb{C}^{N_e N \times 1}$ is a length-$N_e N$ vector of the concatenation of all noisy reconstructed echo images, $\mathbf{F}(\mathbf{x}) = \left[\mathbf{F}_1(\mathbf{x})^T, \ldots, \mathbf{F}_{N_e}(\mathbf{x})^T\right]^T \in \mathbb{C}^{N_e N \times 1}$, α is the regularization parameter, and $\hat{\mathbf{x}}_0$ is a starting initial guess. A preconditioning matrix $\mathbf{W} \in \mathbb{C}^{2N \times 2N}$ contains a Sobolev norm that enforces spatial smoothness on the static off-resonance map:

$$\begin{bmatrix} \boldsymbol{\rho} \\ \Delta\mathbf{f} \end{bmatrix} = \begin{bmatrix} \mathbf{I}_N & \mathbf{0} \\ \mathbf{0} & \mathscr{F}^{-1}\left(1 + w\|\mathbf{k}\|_{\ell_2}^2\right)^{-h} \end{bmatrix} \begin{bmatrix} \widehat{\boldsymbol{\rho}} \\ \widehat{\Delta\mathbf{f}} \end{bmatrix},$$
$$\left(1 + w\|\mathbf{k}\|_{\ell_2}^2\right)^{-h} \widehat{\Delta\mathbf{f}} \triangleq \begin{bmatrix} \left(1 + w\left\|\overrightarrow{k}_1\right\|_{\ell_2}^2\right)^{-h} & 0 & 0 \\ 0 & \ddots & 0 \\ 0 & 0 & \left(1 + w\left\|\overrightarrow{k}_N\right\|_{\ell_2}^2\right)^{-h} \end{bmatrix} \begin{bmatrix} \widehat{\Delta f_1} \\ \vdots \\ \widehat{\Delta f_N} \end{bmatrix}, \quad [19]$$

where $\mathbf{I}_N \in \mathbb{R}^{N \times N}$ is an identity matrix, $\mathscr{F}^{-1} \in \mathbb{C}^{N \times N}$ is a unitary 2D inverse Fourier transform matrix, $\overrightarrow{k} \in \mathbb{R}^{2 \times 1}$ is normalized Cartesian k-space coordinates defined in [−0.5,0.5]×[−0.5,0.5], and $w, h \in \mathbb{R}$ are constants set to 32 and 16, respectively. Equation 18 is solved with the IRGNM (see Appendix).

METHODS

3.1 Reconstruction and image processing

Cartesian and spiral image reconstructions and post-processing were performed in MATLAB R2020b (MathWorks, Natick, MA) on a PC equipped with one 1.60-GHz 4-core Intel i5–8250U CPU and 20 GB of RAM. A vendor proprietary raw data format was converted into the ISMRMRD format (48) and read in MATLAB (49). For both Cartesian and spiral reconstructions, FFT was applied to transform from **k**-space to image-space. Coil sensitivity maps were estimated using the Walsh method (50) from the 32 × 32 Hanning-windowed center of **k**-space data (gridded **k**-space data for spiral acquisitions).

Neither intensity normalization nor gradient nonlinearity correction were applied. Spiral trajectories were generated with (51). A sample density compensation function (52) was computed with (53). NUFFT code was downloaded from (54). MaxGIRF reconstructions were performed with the LSQR algorithm with maximum number of iterations = 15 and tolerance = 1e-5. For static off-resonance map calculation, a coil sensitivity map from the first echo image was used to reconstruct coil-combined images of the other echoes. A smooth static off-resonance map was estimated by the IRGNM with: $\alpha_{\min}$ = 1e-6 (55), GN iterations = 35, maximum number of LSQR iterations = 250, and tolerance of LSQR = 1e-10.

3.2 Selection of an optimal rank *L*

We chose an optimal L that gives less than 2% error in normalized root mean square error (**NRMSE**) between complex-valued full-rank and low-rank reconstructions: $\text{NRMSE} = \|\mathbf{m}_{\text{full}} - \mathbf{m}_{\text{low}}\|_{\ell_2} / \|\mathbf{m}_{\text{full}}\|_{\ell_2}$. In-vivo multi-slice spiral spin-echo axial and slightly oblique sagittal datasets were used for evaluation. A randomized SVD algorithm as described in Supporting Information Text S2 was used to compute the SVD of a higher-order encoding matrix. Singular values up to 50/80 (axial/sagittal) were calculated and considered as full rank. Image reconstructions were performed with a conjugate phase reconstruction, i.e., the right side of Equation 12.

3.3 Numerical simulation

To validate the proposed MaxGIRF approach, noiseless simulations on brain images with simulated 8-channel coil sensitivity maps, 256 × 256 matrix, were performed. A sagittal slice was obtained from a 3D MIDA brain phantom (56) and coil sensitivity maps were obtained from (57). The 116 tissue types of a MIDA phantom were categorized into 13 tissue labels used in a Brainweb phantom (58) by visual matching. MR parameters ($T_1/T_2/T_2^*/M_0$) were obtained from a Brainweb phantom acquired at 1.5 T and the dependence of relaxation parameters on the main magnetic field strength was ignored. A 20-interleaf, variable-density spiral acquisition (9.2 msec readout) was simulated with G_{max} = 24 mT/m, S_{max} = 144 T/m/sec, ADC dwell time = 2.5 μsec, resolution = 0.9375 × 0.9375 mm^2, and FOV decreasing from 240 × 240 mm^2 to 180 × 180 mm^2. The base spiral interleaf was similar to that used in 3D brain MR fingerprinting (59). Direct matrix-vector multiplications using Equations 7 and 8 were used to generate noiseless **k**-space data. System imperfections such as static off-resonance and eddy currents were not simulated. The B0 dependence (0.55T, 1.5T, 3T, 7T) and off-isocenter dependence (z = 0, 50, 100, 150, 200 mm) of concomitant fields were simulated. MaxGIRF reconstructions were performed with a low-rank approximation ($L/L_{\max}$ =50/80) and NUFFT. The NRMSE between a Cartesian reference and spiral reconstructions were calculated. A time-averaged concomitant field map for the first interleaf (in Hz), $f_{c,1}(\mathbf{r})$, over the spiral readout duration (T) was calculated to demonstrate its relative magnitude compared with a static off-resonance map (60):

$$f_{c,\ 1}(\mathbf{r}) = \frac{1}{2\pi T}\sum_{\ell=4}^{N_\ell}\int_0^T h_{\ell,1}(\tau)d\tau\ p_\ell(\mathbf{r}) = \frac{1}{2\pi T}\sum_{\ell=4}^{N_\ell} k_{\ell,1}(T)\ p_\ell(\mathbf{r})\,. \quad [21]$$

3.4 Imaging system

All imaging experiments were performed on a high-performance 0.55T scanner (prototype MAGNETOM Aera, Siemens Healthcare, Erlangen, Germany) with gradients capable of 45 mT/m amplitude and 200 T/m/sec slew rate (35,36). A 16-channel head/neck receive coil was used for phantom and in vivo experiments.

3.5 GIRF measurements

GIRF measurements were obtained using a set of triangular input functions and a spherical phantom as described by (30). A body coil was used for both RF transmission and signal reception. The Brodsky method (26) was used to estimate both B0 cross-terms and first-order self-term GIRFs as described by (32). Only self-term GIRFs were used in this study.

3.6 Phantom experiments

Spiral scans (axial and sagittal) of an ISMRM/NIST system phantom were acquired with a 2D gradient-echo (**GRE**) pulse sequence. An 8-interleaf, uniform-density spiral-out trajectory was designed to have 11.8 ms readout duration. A target axial slice was imaged at isocenter and 75 mm off-isocenter in the z-direction. A sagittal slice was imaged at isocenter. Imaging parameters were: FOV = 224 × 224 mm^2, resolution = 1.4 × 1.4 mm^2, slice thickness = 8 mm, flip angle = 20°, TR = 100 ms, TE = 1 ms, and number of signal averages = 1. Ten repetitions were performed to reach steady-state. For a static off-resonance map, a single-echo 2D Cartesian GRE sequence was repeated to acquire datasets at different echo times (2.5, 3.7, 4.7, 5.7, 6.7, and 7.7 ms).

3.7 Human experiments

All volunteers were scanned under a protocol approved by our local institutional review board (clinicaltrials.gov NCT03331380) and provided written informed consent. In-vivo human brain scans (axial and sagittal) were acquired with a 2D interleaved multi-slice spiral spin-echo pulse sequence. A slice-rephasing gradient and the left crusher of a refocusing pulse were combined with a waveform reshaping technique (61) to minimize the concomitant-field phase. Spoiler gradients were applied on all three axes at the end of a readout. Imaging parameters were: FOV = 240 × 240 mm^2, resolution = 0.75 × 0.75 mm^2, slice thickness = 5 mm, slice gap = 15 mm, flip angle = 90°, TR = 745/500 (spiral/Cartesian) ms, TE = 15 ms, ADC dwell time = 2.5 μsec, readout duration = 11.89 msec, number of readout samples = 4756, number of interleaves = 24, and number of signal averages = 14. For comparison, King's method was used for both axial and sagittal scans. Additionally, a modified King's method including static off-resonance correction was performed for axial scans. Specifically, after correcting a time-varying global frequency offset (through-plane correction of concomitant field-induced phase), frequency-segmented

deblurring was performed for in-plane blurring correction, using an ordinary time parameter and a static off-resonance map for Equations 26 and 30 in Ref (7), respectively.

RESULTS

Figure 2 shows the NRMSEs between full-rank and low-rank reconstructions from in vivo multi-slice spiral spin echo axial and sagittal datasets. NRMSEs are provided as a function of rank L when (A and D) only static off-resonance is included, (B and E) only concomitant fields are included, and (C and F) both static off-resonance and concomitant fields are included in the higher-order encoding matrices. For axial orientation, since the effect of concomitant fields is a time-dependent receive frequency shift, its contribution to the rank is minimal (Figure 2B) and thus the static off-resonance contributes mostly to the rank (Figure 2A). For non-axial orientations, since the effect of concomitant fields is spatiotemporal blurring, a large rank is required compared with that in axial orientation. The rank of static off-resonance is less than 8 like axial orientation and smaller than the rank of concomitant fields in absolute sense (Figure 2D vs 2E). The low-rank (L/L_{max}=8/50) reconstruction in Figure 2C gives almost perfect reconstruction for all axial slices and the low-rank (L/L_{max}=30/80) reconstruction in Figure 2F gives <2% error for all sagittal slices. The signal intensity attenuation is primarily in regions with high off-resonance. The maximum deviation within the brain cortex of the difference between full-rank and low-rank (L=30) reconstructions is <2% for all sagittal slices (only a slice at x = 50.0 mm is shown). The reconstruction time for the non-iterative, conjugate phase-based MaxGIRF (also iterative MaxGIRF) is linearly scaled by the rank, i.e., number of singular values. The reconstruction times per singular value for axial and sagittal orientations were 5 secs and 8 secs, respectively. Thus the reconstruction times (low-rank/full-rank) for axial and sagittal orientations were 40/250 secs (8/50 rank) and 240/640 secs (30/80 rank), respectively.

Figure 3 demonstrates noiseless numerical simulations of MaxGIRF reconstruction, using a low-rank approximation (L/L_{max}=50/80). The NRMSEs for MaxGIRF at x = 0 mm decreased gradually from 8.6% to 8.0% as the field strength increases. This small decrease in NRMSEs is attributed to weaker concomitant fields at higher field strengths and did not make any noticeable difference in image quality. This minimum error (8.6%) is mainly caused by the difference between Cartesian and spiral image reconstructions. Application of MaxGIRF reconstruction on off-isocenter acquisitions achieved this minimum error, indicating perfect correction of the concomitant fields.

Figure 4 shows MaxGIRF reconstruction (L=8) on axial spiral scans of a NIST/ISMRM phantom at 0.55T. The blurring caused by the static off-resonance and concomitant fields is successfully removed as compared to the conventional conjugate gradient based iterative SENSE (**CG-SENSE**) reconstruction. The inclusion of a static off-resonance map in MaxGIRF reconstruction further improves the sharpness of features in regions with non-zero off-resonance.

Figures 5 and 6 compares images reconstructed by MaxGIRF reconstruction (L=8), King's method without static off-resonance correction, and King's method with static off-resonance correction for a slice at z = 17.5 mm and z = 105.0 mm, respectively, from multi-slice axial

spiral spin echo imaging of a healthy volunteer at 0.55T. For non-oblique axial spiral scans, the concomitant fields generate a time-varying global frequency offset and thus King's method removed most spatial blurring. King's method with static off-resonance correction achieved further improvements in regions with slowly varying off-resonance (Figure 6E) and the sharpness in such regions are comparable with MaxGIRF reconstruction. However, it achieved only minor improvements in regions with sharply varying static off-resonance (Figure 5E). Since most noniterative off-resonance methods (62,63) assume that the static off-resonance map varies slowly in space, iterative MaxGIRF reconstruction achieved superior performance compared with King's method with static off-resonance correction, in line with (64). The MaxGIRF reconstruction time was 20 mins per slice with a reconstruction matrix size of 320 × 320.

Figures 7 and 8 compares images reconstructed by NUFFT, King's method (without B0 correction), and MaxGIRF (L=30) for a sagittal slice at x = 0.0 mm and z = 50.0 mm, respectively, from multi-slice spiral spin echo imaging of a healthy volunteer at 0.55T. Because the spine region in Figure 7E is reconstructed without static off-resonance, the improvements by MaxGIRF are solely attributed to the methodological difference between King's method and MaxGIRF. A green box in Figure 8 shows an exemplary region where King's method adversely increases blurring artifacts (compared to NUFFT) when concomitant fields counteract static off-resonance. In contrast, MaxGIRF with static off-resonance correction correctly handles such complex situations. MaxGIRF provides "sharper" delineation of brain tissue boundaries in Figure 8E compared to King's method. The MaxGIRF reconstruction time was 3 hours per slice with a reconstruction matrix size of 640 × 640.

Figure 9 provides a further analysis on MaxGIRF reconstructions including 1) lowest-order (**L**) vs full-order (**F**) concomitant field compensation; and 2) iterative reconstruction (**CG**) vs non-iterative conjugate phase reconstruction (**CP**). The difference between CP-based MaxGIRF (F) and CP-based MaxGIRF (L) was negligible and thus compensating only lowest-order terms is sufficient in this case. Given the system's gradient strength and field strength, it is not surprising that the higher order terms are having a negligible effect. The difference between CG-based MaxGIRF (L) and CP-based MaxGIRF (L) shows mainly aliasing artifacts. The difference between CP-based MaxGIRF (L) and King's method (King) (both non-iterative methods) showed negligible structured artifacts that resemble the shape of concomitant fields at this slice, even in the areas with aliasing artifacts (e.g., face). This indicates that both methods perform robustly under the influence of aliasing and the methodological difference is manifested as the negligible structured artifacts. However, the CP-based MaxGIRF (L) was only able to compensate strong concomitant fields (> 150 Hz, Figure 7H) near the spine (orange box) while King's method showed residual blurring. To further characterize the structured artifacts, noiseless spiral numerical simulations were performed at 0.55T and 3T using the same geometry as the human mid-sagittal scan but with a larger spiral FOV to remove any potential effects of aliasing on the performance of King's method (See Supporting Information Figures S1 and S2). The difference image shows that structured artifacts are of identical shape (oval shape centered at isocenter) regardless of field strength (not shown) and distance from isocenter. This simulation indicates that King's

method performs well within the boundary of the oval shape but gradually deteriorates beyond this boundary. The size of this oval shape is fixed and not a function of neither imaging parameters nor spiral trajectories. The reconstruction times (axial/sagittal) for non-iterative MaxGIRF methods and King's method were 40/240 secs and 10/20 secs, respectively.

DISCUSSION

We have demonstrated that the MaxGIRF higher-order encoding matrix approach can be used to simultaneously correct concomitant fields and off-resonance for spiral acquisitions at 0.55T. This method uses GIRF-based gradient waveform corrections to accurately calculate spatiotemporally varying concomitant field estimates and statis off-resonance maps to generate a hybrid signal equation with variables in the physical and logical coordinate system for image reconstruction. We characterized the accuracy of a low-rank approximation of higher-order encoding matrices to improve reconstruction times with NRMSEs, and implement a randomized SVD to mitigate memory requirements. The MaxGIRF approach provides improved sharpness in regions with large concomitant fields (including off-isocenter) and/or non-zero static off-resonance, compared to King's method. The effectiveness of the proposed method has been demonstrated with numerical simulations, phantom, and in vivo human spiral acquisitions.

Here, we applied MaxGIRF to spiral imaging using a lower field strength (0.55T) MRI system. Concomitant fields effects are increased at lower field strength, higher gradient amplitudes, longer readouts and distance from isocenter. Therefore, this method is generalizable for several other MRI applications including systems with gradient inserts permitting higher peak gradient amplitude, large FOV imaging, and all field-strengths.

The phantom-based GIRF measurements used by the MaxGIRF approach can be a viable alternative to NMR field probes when gradient nonlinearity is not too severe, gradient systems are approximately LTI over the duration of a scan, and models of concomitant fields are well matched to real measurements. We presumed zero gradient nonlinearity but noticed image distortions both in Cartesian and spiral reconstructions (e.g. sagittal slice of the NIST phantom). The concomitant fields derived without gradient nonlinearity may be sufficient for FOVs used in the current study, but a further investigation is required for large-FOV spiral acquisitions (e.g., cardiac, abdominal, or fetal imaging) especially in large bore MR systems or MR systems with a high-performance gradient insert (34,65–67). Because gradient nonlinearity along each gradient direction can be modeled by a product of spherical harmonics (68,69) and a linear gradient normalized by a reference gradient (70,71), concomitant field terms incorporating the spherical harmonics expansion (possibly up to 9^{th} order) (72) of gradient nonlinearity could be derived following the approach described in (18). Because gradient nonlinearity and a new set of concomitant fields under gradient nonlinearity are a function of linear gradients, both could be predicted by phantom-based GIRFs with high accuracy and incorporated within the MaxGIRF framework.

An optimal rank criterion should depend on the specific MR application. In this study, we choose an optimal rank that gives less than 2% error in both magnitude and phase NRMSEs.

This stringent requirement can be relaxed when signal intensity in regions with high off-resonance (e.g., fat regions) may not be of interest. In the case of water-fat separated imaging or when fat suppression is used, the static off-resonance map may become smoother because the discrete water/fat chemical shift is removed. In this case, the optimal rank may be lower because singular values of smoother images decay more rapidly (73).

One notable advantage of the MaxGIRF approach is that it can be easily adapted to many clinical sites without NMR field probes. MaxGIRF only requires good analytic models of concomitant fields and GIRFs measured with a simple pulse sequence and a spherical phantom. Because analytic expressions of concomitant fields for asymmetric gradient coils can be derived (74), the MaxGIRF approach would be applicable to clinical systems with asymmetric gradient coils that have well-documented analytic expressions. Pulse sequences for GIRF measurements can be developed and shared via a vendor-independent pulse sequence framework (e.g., Pulseq and TOPPE) (75,76). This would enable clinical sites without expertise in sequence programming to obtain GIRF measurements on their own scanners. Note that a pulse sequence for GIRF measurements described in (23) is provided by TOPPE (77). Because of its simple reconstruction procedure, the MaxGIRF approach can be easily integrated into any existing gridding or NUFFT based non-Cartesian reconstruction routines provided in open-source reconstruction platforms such as BART (78), Gadgetron (79), and GPI (80). Therefore, reconstruction software can potentially be shared among sites without difficulty.

This work has several limitations. We did not consider acquisitions where an accumulated concomitant phase affects the net phase of spin isochromats after following excitation or refocusing pulses. This specifically includes balanced steady-state free precession and fast spin echo sequences, each of which may require additional assumptions (e.g., a perfect 180 refocusing pulse for fast spin echo) or additional pulse sequence modifications to formulate a tractable forward model that can be solved with an extension of the MaxGIRF framework.

Another drawback is reconstruction time. The SVD needs to be computed for each subject with a unique static off-resonance map and whenever a slice prescription is changed. The SVD computation time was 1 and 6 mins for axial and sagittal scans, respectively, using a non-parallelized implementation. However, this long computation time could be reduced by switching from a CPU-based randomized SVD implementation (used in this study) to one implemented in parallel architectures such as Graphical Processing Units (**GPUs**). The other computation bottleneck is L repetitions of NUFFTs. Because the current MATLAB implementation does not utilize parallel computing via multicore CPUs, MaxGIRF reconstruction is relatively slow (L times longer than CG-SENSE). This limitation could be partially overcome with simultaneous computations of $L \times N_i$ NUFFTs using multiple GPUs. This may be particularly beneficial for 3D spiral and/or very high-resolution spiral scans.

CONCLUSION

We demonstrate a higher-order image reconstruction method, called MaxGIRF, that incorporates concomitant fields and GIRF-based gradient waveform prediction for spoiled

gradient echo and spin echo spiral imaging. Simulations indicate that MaxGIRF successfully mitigates local blurring caused by concomitant fields at various field strengths and distances from isocenter. MaxGIRF was able to mitigate concomitant fields both in phantom and in vivo brain spiral imaging at 0.55T, superior to the most notable existing solution. Including an accurate static off-resonance map further improves its performance in regions with large static off-resonance. The impact of this method is greatest when imaging with longer readouts, high gradient amplitudes and/or at lower field strength.

Supplementary Material

Refer to Web version on PubMed Central for supplementary material.

ACKNOWLEDGEMENTS

This work was supported by NSF #1828763, NIH R01-HL130494, and the NHLBI DIR (Z01-HL006257). We would like to acknowledge the assistance of Siemens Healthcare in the modification of the MRI system for operation at 0.55T under an existing cooperative research agreement between NHLBI and Siemens Healthcare.

Grant Support: National Science Foundation #1828736; NIH R01-HL130494, and the NHLBI DIR (Z01-HL006257)

Appendix

The nonlinear signal model $\mathbf{G}(\hat{\mathbf{x}})$ is first linearized with the Taylor expansion around the current estimate $\hat{\mathbf{x}}_n$:

$$\mathbf{G}(\hat{\mathbf{x}}_n + \mathbf{d}\hat{\mathbf{x}}) \approx \mathbf{G}(\hat{\mathbf{x}}_n) + \widehat{D}\mathbf{G}(\hat{\mathbf{x}}_n)\mathbf{d}\hat{\mathbf{x}}, \quad [A1]$$

where $\widehat{D}\mathbf{G}(\hat{\mathbf{x}}_n) = \left[\frac{\partial \mathbf{G}}{\partial \hat{\boldsymbol{\rho}}} \; \frac{\partial \mathbf{G}}{\partial \widehat{\Delta \mathbf{f}}}\right]$ is the Fréchet derivative of $\mathbf{G}$ evaluated at $\hat{\mathbf{x}}_n$. Substituting $\hat{\mathbf{x}}$ with $\hat{\mathbf{x}}_n + \mathbf{d}\hat{\mathbf{x}}$ in Equation 18 leads to the cost function that provides the update $\mathbf{d}\hat{\mathbf{x}}$ for the $\boldsymbol{n}$-th Gauss-Newton iteration $\hat{\mathbf{x}}_{n+1} = \hat{\mathbf{x}}_n + \mathbf{d}\hat{\mathbf{x}}$:

$$\Phi(\mathbf{d}\hat{\mathbf{x}}) = \underset{\mathbf{d}\hat{\mathbf{x}}}{\operatorname{argmin}} \|\mathbf{y} - \mathbf{G}(\hat{\mathbf{x}}_n) - \widehat{D}\mathbf{G}(\hat{\mathbf{x}}_n)\mathbf{d}\hat{\mathbf{x}}\|_{\ell_2}^2 + \alpha_n \|\hat{\mathbf{x}}_n + \mathbf{d}\hat{\mathbf{x}} - \hat{\mathbf{x}}_0\|_{\ell_2}^2 . \quad [A2]$$

Equation A2 can be simplified to

$$\left(\left[\widehat{D}\mathbf{G}(\hat{\mathbf{x}}_n)\right]^H \widehat{D}\mathbf{G}(\hat{\mathbf{x}}_n) + \alpha_n \mathbf{I}_{2N}\right)\mathbf{d}\hat{\mathbf{x}} = \left[\widehat{D}\mathbf{G}(\hat{\mathbf{x}}_n)\right]^H (\mathbf{y} - \mathbf{G}(\hat{\mathbf{x}}_n)) + \alpha_n(\hat{\mathbf{x}}_n - \hat{\mathbf{x}}_0) . \quad [A3]$$

Since $\widehat{D}\mathbf{G}(\hat{\mathbf{x}}) \triangleq \frac{d}{d\hat{\mathbf{x}}}\mathbf{G}(\hat{\mathbf{x}}) = \frac{d}{d\hat{\mathbf{x}}}\mathbf{F}(\mathbf{x}) = \frac{d}{d\mathbf{x}}\mathbf{F}(\mathbf{x})\frac{d\mathbf{x}}{d\hat{\mathbf{x}}} = D\mathbf{F}(\mathbf{x})\mathbf{W}$, Equation A3 can be expressed in terms of $D\mathbf{F}(\mathbf{x}_n)$ and solved with LSQR:

$$\left(\mathbf{W}^H\left[D\mathbf{F}(\mathbf{x}_n)\right]^H D\mathbf{F}(\mathbf{x}_n)\mathbf{W} + \alpha_n \mathbf{I}_{2N}\right)\mathbf{d}\hat{\mathbf{x}} = \mathbf{W}^H\left[D\mathbf{F}(\mathbf{x}_n)\right]^H (\mathbf{y} - \mathbf{F}(\mathbf{x}_n)) + \alpha_n(\hat{\mathbf{x}}_n - \hat{\mathbf{x}}_0) . \quad [A4]$$

The regularization parameter is set to decrease per iteration as $\alpha_n = \alpha_0 q^n$, where $q = 2/3$, until it reaches a minimum regularization parameter $\alpha_{\min}$. The data vector $\mathbf{y} \in \mathbb{C}^{N_e N \times 1}$ is scaled to have "100.0 L2 norm" (81) and scaling of unknowns is not used. The derivative operator $D\mathbf{F}(\mathbf{x}) \in \mathbb{C}^{N_e N \times 2N}$ is defined as:

$$DF(\mathbf{x}) = \begin{bmatrix} \frac{\partial F}{\partial \boldsymbol{\rho}} & \frac{\partial F}{\partial \Delta \mathbf{f}} \end{bmatrix} = \begin{bmatrix} \frac{\partial \mathbf{F}_1}{\partial \boldsymbol{\rho}} & \frac{\partial \mathbf{F}_1}{\partial \Delta \mathbf{f}} \\ \vdots & \vdots \\ \frac{\partial \mathbf{F}_{N_e}}{\partial \boldsymbol{\rho}} & \frac{\partial \mathbf{F}_{N_e}}{\partial \Delta \mathbf{f}} \end{bmatrix} = \begin{bmatrix} \operatorname{diag}(\exp(j2\pi \Delta \mathbf{f} \mathrm{TE}_1)) & \operatorname{diag}(\boldsymbol{\rho}) \operatorname{diag}(\exp(j2\pi \Delta \mathbf{f} \mathrm{TE}_1))(j2\pi \mathrm{TE}_1) \\ \vdots & \vdots \\ \operatorname{diag}\left(\exp\left(j2\pi \Delta \mathbf{f} \mathrm{TE}_{N_e}\right)\right) & \operatorname{diag}(\boldsymbol{\rho}) \operatorname{diag}\left(\exp\left(j2\pi \Delta \mathbf{f} \mathrm{TE}_{N_e}\right)\right)\left(j2\pi \mathrm{TE}_{N_e}\right) \end{bmatrix}. \quad [A5]$$

Using Equation A5, the matrix-vector product $\mathbf{dy} = D\mathbf{F}(\mathbf{x})\mathbf{W}\mathbf{d}\hat{\mathbf{x}} \in \mathbb{C}^{N_e N \times 1}$ is calculated as:

$$\mathbf{dy} = \begin{bmatrix} \mathbf{dy}_1 \\ \vdots \\ \mathbf{dy}_{N_e} \end{bmatrix} = DF(\mathbf{x}) \begin{bmatrix} \mathbf{d}\boldsymbol{\rho} \\ \mathbf{d}\Delta \mathbf{f} \end{bmatrix} = \begin{bmatrix} \operatorname{diag}(\boldsymbol{\psi}_1)\mathbf{d}\boldsymbol{\rho} + \operatorname{diag}(\boldsymbol{\rho}) \operatorname{diag}(\boldsymbol{\psi}_1)(j2\pi \mathrm{TE}_1)\mathbf{d}\Delta \mathbf{f} \\ \vdots \\ \operatorname{diag}\left(\boldsymbol{\psi}_{N_e}\right)\mathbf{d}\boldsymbol{\rho} + \operatorname{diag}(\boldsymbol{\rho}) \operatorname{diag}\left(\boldsymbol{\psi}_{N_e}\right)\left(j2\pi \mathrm{TE}_{N_e}\right)\mathbf{d}\Delta \mathbf{f} \end{bmatrix}, \quad [A6]$$

where we define $\boldsymbol{\psi}_m = \exp(j2\pi \Delta \mathbf{f} \mathrm{TE}_m)$. Similarly, the matrix-vector product $\mathbf{dx} = [D\mathbf{F}(\mathbf{x})]^H \mathbf{dy} \in \mathbb{C}^{2N \times 1}$ involving the adjoint of the derivative operator can be calculated as:

$$\mathbf{dy} = \begin{bmatrix} \mathbf{d}\boldsymbol{\rho} \\ \mathbf{d}\Delta \mathbf{f} \end{bmatrix} = [D\mathbf{F}(\mathbf{x})]^H \begin{bmatrix} \mathbf{dy}_1 \\ \vdots \\ \mathbf{dy}_{N_e} \end{bmatrix} = \begin{bmatrix} \sum_{m=1}^{N_e} \operatorname{diag}(\boldsymbol{\psi}_m^*)\mathbf{dy}_m \\ \Re\left\{ \sum_{m=1}^{N_e} \operatorname{diag}(\boldsymbol{\rho}) \operatorname{diag}(\boldsymbol{\psi}_m^*)(-j2\pi \mathrm{TE}_m)\mathbf{dy}_m \right\} \end{bmatrix}, \quad [A7]$$

where $\Re\{\cdot\}$ denotes the real operator that keeps only the real part of a complex-valued input.

DATA AVAILABILITY STATEMENT

The code and sample data (ISMRMRD format) that support the findings of this study are openly available in GitHub at https://www.github.com/usc-mrel/lowfield_maxgirf and https://www.github.com/usc-mrel/nlinv_estimation.

REFERENCES

1. Li Z, Hu HH, Miller JH, et al. A spiral spin-echo MR imaging technique for improved flow artifact suppression in T1-weighted postcontrast brain imaging: A comparison with Cartesian turbo spin-echo. In: American Journal of Neuroradiology.; 2016. doi: 10.3174/ajnr.A4600.
2. Ooi MB, Li Z, Robison RK, et al. Spiral T1 spin-echo for routine postcontrast brain MRI exams: A multicenter multireader clinical evaluation. Am. J. Neuroradiol. 2020 doi: 10.3174/ajnr.A6409.
3. Ma D, Gulani V, Seiberlich N, et al. Magnetic resonance fingerprinting. Nature 2013;495:187–192 doi: 10.1038/nature11971. [PubMed: 23486058]
4. Jiang Y, Ma D, Seiberlich N, Gulani V, Griswold MA. MR fingerprinting using fast imaging with steady state precession (FISP) with spiral readout. Magn. Reson. Med. 2015 doi: 10.1002/mrm.25559.
5. Nayak KS, Hargreaves BA, Hu BS, Nishimura DG, Pauly JM, Meyer CH. Spiral Balanced Steady-State Free Precession Cardiac Imaging. 2005;1473:1468–1473 doi: 10.1002/mrm.20489.
6. Bernstein MA, Zhou XJ, Polzin JA, et al. Concomitant gradient terms in phase contrast MR: Analysis and correction. Magn. Reson. Med. 1998;39:300–308 doi: 10.1002/mrm.1910390218. [PubMed: 9469714]
7. King KF, Ganin A, Zhou XJ, Bernstein MA. Concomitant gradient field effects in spiral scans. Magn. Reson. Med. 1999;41:103–112 doi: 10.1002/(SICI)1522-2594(199901)41:1<103::AID-MRM15>3.0.CO;2-M. [PubMed: 10025617]
8. Chen W, Sica CT, Meyer CH. Fast conjugate phase image reconstruction based on a Chebyshev approximation to correct for B0 field inhomogeneity and concomitant gradients. Magn. Reson. Med. 2008 doi: 10.1002/mrm.21703.
9. Cheng JY, Santos JM, Pauly JM. Fast concomitant gradient field and field inhomogeneity correction for spiral cardiac imaging. Magn. Reson. Med. 2011;66:390–401 doi: 10.1002/mrm.22802. [PubMed: 21384423]
10. Cheng JY, Santos JM, Pauly JM. Fast concomitant gradient field and field inhomogeneity correction for spiral cardiac imaging. Magn. Reson. Med. 2011 doi: 10.1002/mrm.22802.
11. Wilm BJ, Barmet C, Pavan M, Pruessmann KP. Higher order reconstruction for MRI in the presence of spatiotemporal field perturbations. Magn. Reson. Med. 2011;65:1690–1701 doi: 10.1002/mrm.22767. [PubMed: 21520269]
12. De Zanche N, Barmet C, Nordmeyer-Massner JA, Pruessmann KP. NMR Probes for measuring magnetic fields and field dynamics in MR systems. Magn. Reson. Med. 2008;60:176–186 doi: 10.1002/mrm.21624. [PubMed: 18581363]
13. Barmet C, De Zanche N, Pruessmann KP. Spatiotemporal magnetic field monitoring for MR. Magn. Reson. Med. 2008;60:187–97 doi: 10.1002/mrm.21603. [PubMed: 18581361]
14. Wilm BJ, Barmet C, Gross S, et al. Single-Shot Spiral Imaging Enabled by an Expanded Encoding Model : Demonstration in Diffusion MRI. 2017;91:83–91 doi: 10.1002/mrm.26493.
15. Engel M, Kasper L, Barmet C, et al. Single-shot spiral imaging at 7 T. Magn. Reson. Med. 2018;80:1836–1846 doi: 10.1002/mrm.27176. [PubMed: 29575161]
16. Dietrich BE, Brunner DO, Wilm BJ, et al. A field camera for MR sequence monitoring and system analysis. Magn. Reson. Med. 2016;75:1831–1840 doi: 10.1002/mrm.25770. [PubMed: 25975352]
17. Barmet C, De Zanche N, Wilm BJ, Pruessmann KP. A transmit/receive system for magnetic field monitoring of in vivo MRI. Magn. Reson. Med. 2009 doi: 10.1002/mrm.21996.
18. Testud F, Gallichan D, Layton KJ, et al. Single-shot imaging with higher-dimensional encoding using magnetic field monitoring and concomitant field correction. Magn. Reson. Med. 2015;73:1340–1357 doi: 10.1002/mrm.25235. [PubMed: 24687529]
19. Sipilä P, Lange D, Lechner S, et al. Robust susceptibility-matched NMR probes for compensation of gradient field imperfections in magnetic resonance imaging. TRANSDUCERS EUROSENSORS '07 – 4th Int. Conf. Solid-State Sensors, Actuators Microsystems 2007;146:2381–2384 doi: 10.1109/SENSOR.2007.4300649.
20. Sipilä P, Greding S, Wachutka G, Wiesinger F. 2H transmit-receive NMR probes for magnetic field monitoring in MRI. Magn. Reson. Med. 2011 doi: 10.1002/mrm.22741.

21. Liu H, Matson GB. Accurate measurement of magnetic resonance imaging gradient characteristics. Materials (Basel). 2014;7:1–15 doi: 10.3390/ma7010001. [PubMed: 25343017]
22. Addy NO, Wu HH, Nishimura DG. Simple method for MR gradient system characterization and k-space trajectory estimation. Magn. Reson. Med. 2012;68:120–129 doi: 10.1002/mrm.23217. [PubMed: 22189904]
23. Vannesjo SJ, Haeberlin M, Kasper L, et al. Gradient system characterization by impulse response measurements with a dynamic field camera. Magn. Reson. Med. 2013;69:583–93 doi: 10.1002/mrm.24263. [PubMed: 22499483]
24. Vannesjo SJ, Graedel NN, Kasper L, et al. Image reconstruction using a gradient impulse response model for trajectory prediction. Magn. Reson. Med. 2016;76:45–58 doi: 10.1002/mrm.25841. [PubMed: 26211410]
25. Duyn JH, Yang Y, Frank JA, Van Der Veen JW. Simple Correction Method for k-Space Trajectory Deviations in MRI The new method measures the actual k-space trajectories. J. Magn. Reson. 1998;132:150–153. [PubMed: 9615415]
26. Brodsky EK, Klaers JL, Samsonov AA, Kijowski R, Block WF. Rapid measurement and correction of phase errors from B0 eddy currents: Impact on image quality for non-cartesian imaging. Magn. Reson. Med. 2013;69:509–515 doi: 10.1002/mrm.24264. [PubMed: 22488532]
27. Malik SJ, Hajnal JV. Phase Relaxed Localized Excitation Pulses for Inner Volume Fast Spin Echo Imaging. 2016;3:848–861 doi: 10.1002/mrm.25996.
28. Abo Seada S, Price AN, Schneider T, Hajnal JV., Malik SJ. Multiband RF pulse design for realistic gradient performance. Magn. Reson. Med. 2019 doi: 10.1002/mrm.27411.
29. Bruijnen T, Stemkens B, van den Berg CAT, Tijssen RHN. Prospective GIRF-based RF phase cycling to reduce eddy current-induced steady-state disruption in bSSFP imaging. Magn. Reson. Med. 2020 doi: 10.1002/mrm.28097.
30. Campbell-Washburn AE, Xue H, Lederman RJ, Faranesh AZ, Hansen MS. Real-time distortion correction of spiral and echo planar images using the gradient system impulse response function. Magn. Reson. Med. 2016;75:2278–2285 doi: 10.1002/mrm.25788. [PubMed: 26114951]
31. Stich M, Wech T, Slawig A, et al. Gradient waveform pre-emphasis based on the gradient system transfer function. Magn. Reson. Med. 2018;80:1521–1532 doi: 10.1002/mrm.27147. [PubMed: 29479736]
32. Robison RK, Li Z, Wang D, Ooi MB, Pipe JG. Correction of B 0 eddy current effects in spiral MRI. Magn. Reson. Med. 2019 doi: 10.1002/mrm.27583.
33. Meier C, Zwanger M, Feiweier T, Porter D. Concomitant field terms for asymmetric gradient coils: Consequences for diffusion, flow, and echo-planar imaging. Magn. Reson. Med. 2008 doi: 10.1002/mrm.21615.
34. Wilm BJ, Hennel F, Roesler MB, Weiger M, Pruessmann KP. Minimizing the echo time in diffusion imaging using spiral readouts and a head gradient system. Magn. Reson. Med. 2020 doi: 10.1002/mrm.28346.
35. Campbell-Washburn AE, Ramasawmy R, Restivo MC, et al. Opportunities in interventional and diagnostic imaging by using high-performance low-field-strength MRI. Radiology 2019 doi: 10.1148/radiol.2019190452.
36. Restivo MC, Ramasawmy R, Bandettini WP, Herzka DA, Campbell-Washburn AE. Efficient spiral in-out and EPI balanced steady-state free precession cine imaging using a high-performance 0.55T MRI. Magn. Reson. Med. 2020 doi: 10.1002/mrm.28278.
37. Schultz G, Ullmann P, Lehr H, Welz AM, Hennig J, Zaitsev M. Reconstruction of MRI data encoded with arbitrarily shaped, curvilinear, nonbijective magnetic fields. Magn. Reson. Med. 2010;64:1390–1403 doi: 10.1002/mrm.22393. [PubMed: 20848635]
38. Jung Y, Jashnani Y, Kijowski R, Block WF. Consistent non-Cartesian off-axis MRI quality: Calibrating and removing multiple sources of demodulation phase errors. Magn. Reson. Med. 2007;57:206–211 doi: 10.1002/mrm.21092. [PubMed: 17139618]
39. Tao S, Trzasko JD, Shu Y, Huston J, Bernstein MA. Integrated image reconstruction and gradient nonlinearity correction. Magn. Reson. Med. 2015;74:1019–1031 doi: 10.1002/mrm.25487. [PubMed: 25298258]

40. Paige CC, Saunders MA. LSQR: An Algorithm for Sparse Linear Equations and Sparse Least Squares. ACM Trans. Math. Softw. 1982;8:43–71 doi: 10.1145/355984.355989.
41. Wilm BJ, Barmet C, Pruessmann KP. Fast higher-order MR image reconstruction using singular-vector separation. IEEE Trans. Med. Imaging 2012 doi: 10.1109/TMI.2012.2190991.
42. Fessler JA, Lee S, Olafsson VT, Shi HR, Noll DC. Toeplitz-based iterative image reconstruction for MRI with correction for magnetic field inhomogeneity. IEEE Trans. Signal Process. 2005;53:3393–3402 doi: 10.1109/TSP.2005.853152.
43. Eckart CYG. 311_1.Tif. Psychometrika 1936;1:211–218.
44. Rasche V, Proksa R, Sinkus R, Börnert P, Eggers H. Resampling of data between arbitrary grids using convolution interpolation. IEEE Trans. Med. Imaging 1999;18:385–392 doi: 10.1109/42.774166. [PubMed: 10416800]
45. Fessler JA, Sutton BP. Nonuniform fast Fourier transforms using min-max interpolation. IEEE Trans. Signal Process. 2003;51:560–574 doi: 10.1109/TSP.2002.807005.
46. Tan Z, Voit D, Kollmeier JM, Uecker M, Frahm J. Dynamic water/fat separation and B0 inhomogeneity mapping—joint estimation using undersampled triple-echo multi-spoke radial FLASH. Magn. Reson. Med. 2019;82:1000–1011 doi: 10.1002/mrm.27795. [PubMed: 31033051]
47. Uecker M, Hohage T, Block KT, Frahm J. Image Reconstruction by Regularized Nonlinear Inversion — Joint Estimation of Coil Sensitivities and Image Content. 2008;682:674–682 doi: 10.1002/mrm.21691.
48. https://github.com/ismrmrd/siemens_to_ismrmrd.
49. https://github.com/ismrmrd/ismrmrd.
50. Walsh DO, Gmitro AF, Marcellin MW. Adaptive reconstruction of phased array MR imagery. Magn. Reson. Med. 2000;43:682–690 doi: 10.1002/(SICI)1522-2594(200005)43:5<682::AID-MRM10>3.0.CO;2-G. [PubMed: 10800033]
51. http://www-mrsrl.stanford.edu/#brian/vdspiral/.
52. Zwart NR, Johnson KO, Pipe JG. Efficient sample density estimation by combining gridding and an optimized kernel. Magn. Reson. Med. 2012;67:701–710 doi: 10.1002/mrm.23041. [PubMed: 21688320]
53. https://github.com/ISMRM/mri_unbound.
54. https://github.com/JeffFessler/mirt.
55. Wang X, Kohler F, Unterberg-Buchwald C, Lotz J, Frahm J, Uecker M. Model-based myocardial T1 mapping with sparsity constraints using single-shot inversion-recovery radial FLASH cardiovascular magnetic resonance. J. Cardiovasc. Magn. Reson. 2019;21:1–11 doi: 10.1186/s12968-019-0570-3. [PubMed: 30612574]
56. Iacono MI, Neufeld E, Akinnagbe E, et al. MIDA: A multimodal imaging-based detailed anatomical model of the human head and neck. PLoS One 2015 doi: 10.1371/journal.pone.0124126.
57. https://github.com/hansenms/ismrm_sunrise_matlab.
58. Collins DL, Zijdenbos AP, Kollokian V, et al. Design and construction of a realistic digital brain phantom. IEEE Trans. Med. Imaging 1998;17:463–468 doi: 10.1109/42.712135. [PubMed: 9735909]
59. Cao X, Ye H, Liao C, Li Q, He H, Zhong J. Fast 3D brain MR fingerprinting based on multi-axis spiral projection trajectory. Magn. Reson. Med. 2019;82:289–301 doi: 10.1002/mrm.27726. [PubMed: 30883867]
60. Wang Y, van Gelderen P, de Zwart JA, Campbell-Washburn AE, Duyn JH. FMRI based on transition-band balanced SSFP in comparison with EPI on a high-performance 0.55 T scanner. Magn. Reson. Med. 2021;85:3196–3210 doi: 10.1002/mrm.28657. [PubMed: 33480108]
61. Zhou XJ, Tan SG, Bernstein MA. Artifacts induced by concomitant magnetic field in fast spin-echo imaging. Magn. Reson. Med. 1998;40:582–591 doi: 10.1002/mrm.1910400411. [PubMed: 9771575]
62. Noll DC, Meyer CH, Pauly JM, Nishimura DG, Macovski A. A Homogeneity Correction Method for Magnetic Resonance Imaging with Time-Vaiying Gradients. IEEE Trans. Med. Imaging 1991;10:629–637 doi: 10.1109/42.108599. [PubMed: 18222870]

63. Ahunbay E, Pipe JG. Rapid method for deblurring spiral MR images. Magn. Reson. Med. 2000;44:491–494 doi: 10.1002/1522-2594(200009)44:3<491::AID-MRM22>3.0.CO;2-Z. [PubMed: 10975904]
64. Makhijani MK, Nayak KS. Exact correction of sharply varying off-resonance effects in spiral MRI. In: 2006 3rd IEEE International Symposium on Biomedical Imaging: From Nano to Macro - Proceedings. Vol. 2006.; 2006. pp. 730–733. doi: 10.1109/isbi.2006.1625020.
65. Weiger M, Overweg J, Rösler MB, et al. A high-performance gradient insert for rapid and short-T2 imaging at full duty cycle. Magn. Reson. Med. 2018;79:3256–3266 doi: 10.1002/mrm.26954. [PubMed: 28983969]
66. Foo TKF, Laskaris E, Vermilyea M, et al. Lightweight, compact, and high-performance 3T MR system for imaging the brain and extremities. Magn. Reson. Med. 2018;80:2232–2245 doi: 10.1002/mrm.27175. [PubMed: 29536587]
67. Hennel F, Wilm B, Roesler MB, Weiger M, Dietrich B, Pruessmann KP. Echo-planar imaging of the human head with 100 mT/m gradients and high-order modeling of eddy current fields. Magn. Reson. Med. 2020;84:751–761 doi: 10.1002/mrm.28168. [PubMed: 31961966]
68. Roméo F, Hoult DI. Magnet field profiling: Analysis and correcting coil design. Magn. Reson. Med. 1984;1:44–65 doi: 10.1002/mrm.1910010107. [PubMed: 6571436]
69. Janke A, Zhao H, Cowin GJ, Galloway GJ, Doddrell DM. Use of spherical harmonic deconvolution methods to compensate for nonlinear gradient effects on MRI images. Magn. Reson. Med. 2004;52:115–122 doi: 10.1002/mrm.20122. [PubMed: 15236374]
70. Bammer R, Markl M, Barnett A, et al. Analysis and generalized correction of the effect of spatial gradient field distortions in diffusion-weighted imaging. Magn. Reson. Med. 2003;50:560–569 doi: 10.1002/mrm.10545. [PubMed: 12939764]
71. Markl M, Bammer R, Alley MT, et al. Generalized reconstruction of phase contrast MRI: Analysis and correction of the effect of gradient field distortions. Magn. Reson. Med. 2003;50:791–801 doi: 10.1002/mrm.10582. [PubMed: 14523966]
72. Weavers PT, Tao S, Trzasko JD, et al. Image-based gradient non-linearity characterization to determine higher-order spherical harmonic coefficients for improved spatial position accuracy in magnetic resonance imaging. Magn. Reson. Imaging 2017;38:54–62 doi: 10.1016/j.mri.2016.12.020. [PubMed: 28034637]
73. A R. SVD Based Image Processing Applications: State of The Art, Contributions and Research Challenges. Int. J. Adv. Comput. Sci. Appl. 2012;3:26–34 doi: 10.14569/ijacsa.2012.030703.
74. Meier C, Zwanger M, Feiweier T, Porter D. Concomitant field terms for asymmetric gradient coils: Consequences for diffusion, flow, and echo-planar imaging. Magn. Reson. Med. 2008;60:128–134 doi: 10.1002/mrm.21615. [PubMed: 18581353]
75. Layton KJ, Kroboth S, Jia F, et al. Pulseq : A Rapid and Hardware-Independent Pulse Sequence Prototyping Framework. 2017;1552:1544–1552 doi: 10.1002/mrm.26235.
76. Nielsen J, Noll DC. TOPPE : A Framework for Rapid Prototyping of MR Pulse Sequences. 2018;3134:3128–3134 doi: 10.1002/mrm.26990.
77. https://github.com/toppeMRI/old_matlab/tree/oldOct2018/examples/v2/girf.
78. Generalized Magnetic Resonance Image Reconstruction using The Berkeley Advanced Reconstruction Toolbox. 2015;2486:9660006 doi: 10.5281/zenodo.31907.
79. Hansen MS, Sørensen TS. Gadgetron: An open source framework for medical image reconstruction. Magn. Reson. Med. 2013;69:1768–1776 doi: 10.1002/mrm.24389. [PubMed: 22791598]
80. Zwart NR, Pipe JG. Graphical programming interface: A development environment for MRI methods. Magn. Reson. Med. 2015;74:1449–1460 doi: 10.1002/mrm.25528. [PubMed: 25385670]
81. Uecker M, Zhang S, Frahm J. Nonlinear inverse reconstruction for real-time MRI of the human heart using undersampled radial FLASH. Magn. Reson. Med. 2010;63:1456–1462 doi: 10.1002/mrm.22453. [PubMed: 20512847]

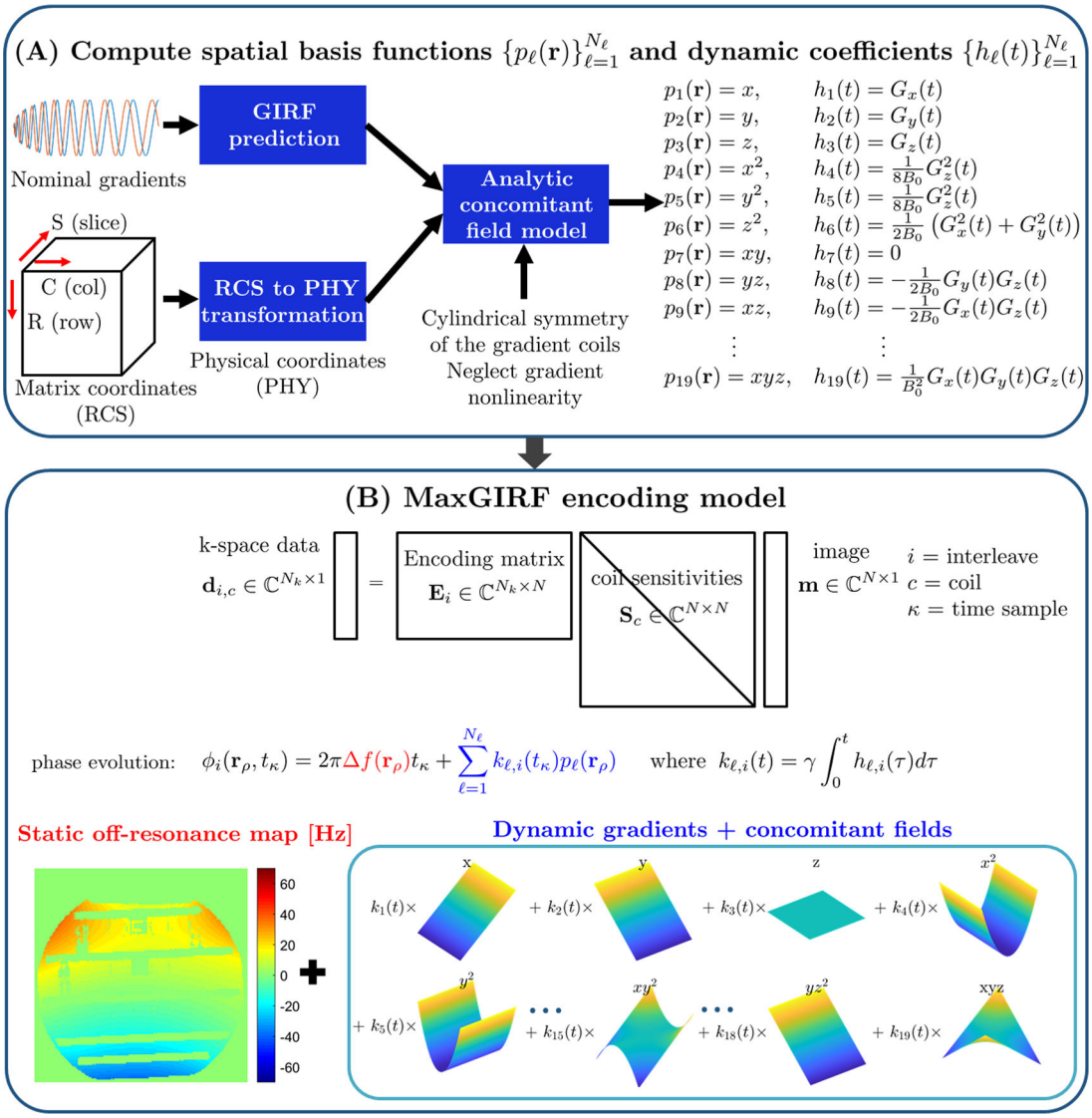

Figure 1.

MaxGIRF reconstruction flowchart. (A) Computation of concomitant field model: Gradient waveforms in the logical coordinate system are first transformed into the physical coordinate system. Distorted gradients in the physical coordinate system are estimated by GIRFs. Analytic expressions of concomitant fields derived from the coil geometry, presumed gradient nonlinearity, and GIRF-predicted gradients, are calculated for each spatial position in the physical coordinate system. (B) Encoding model: The MaxGIRF encoding model is an extension of the SENSE model that additionally includes phase terms due to static off-resonance and concomitant fields. The phase evolution per voxel is represented as the sum of phase contributions from static off-resonance (red) and spatial basis functions (blue) that includes both linear gradients and concomitant field terms.

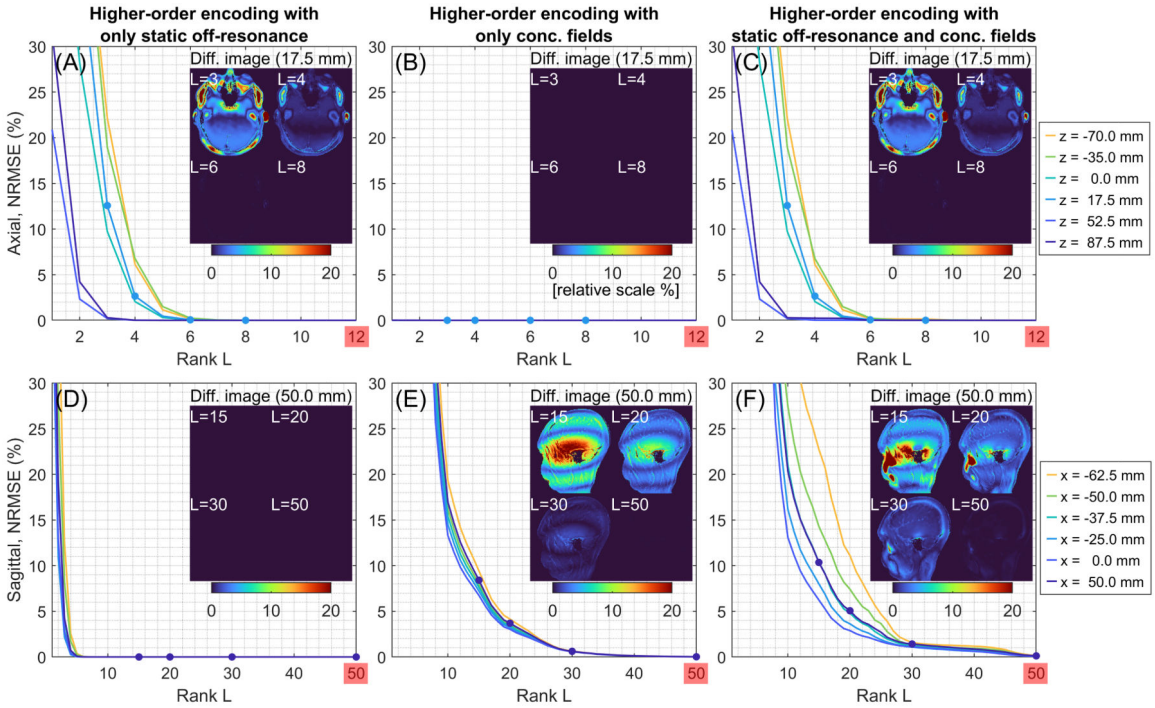

Figure 2.

Low-rank approximations of the MaxGIRF higher-order encoding matrix are effective. NRMSEs are measured between full-rank image reconstructions and low-rank approximations from in vivo multi-slice spiral spin echo axial and sagittal datasets. NRMSEs when (A and D) only static off-resonance is included, (B and E) only concomitant fields are included, (C and F) both static off-resonance and concomitant fields are included in the higher-order encoding matrices. The inset images show the difference between full-rank (50/80 for axial/sagittal) and *L*-rank reconstructions. Note that a different range of the x-axis is used for clarity.

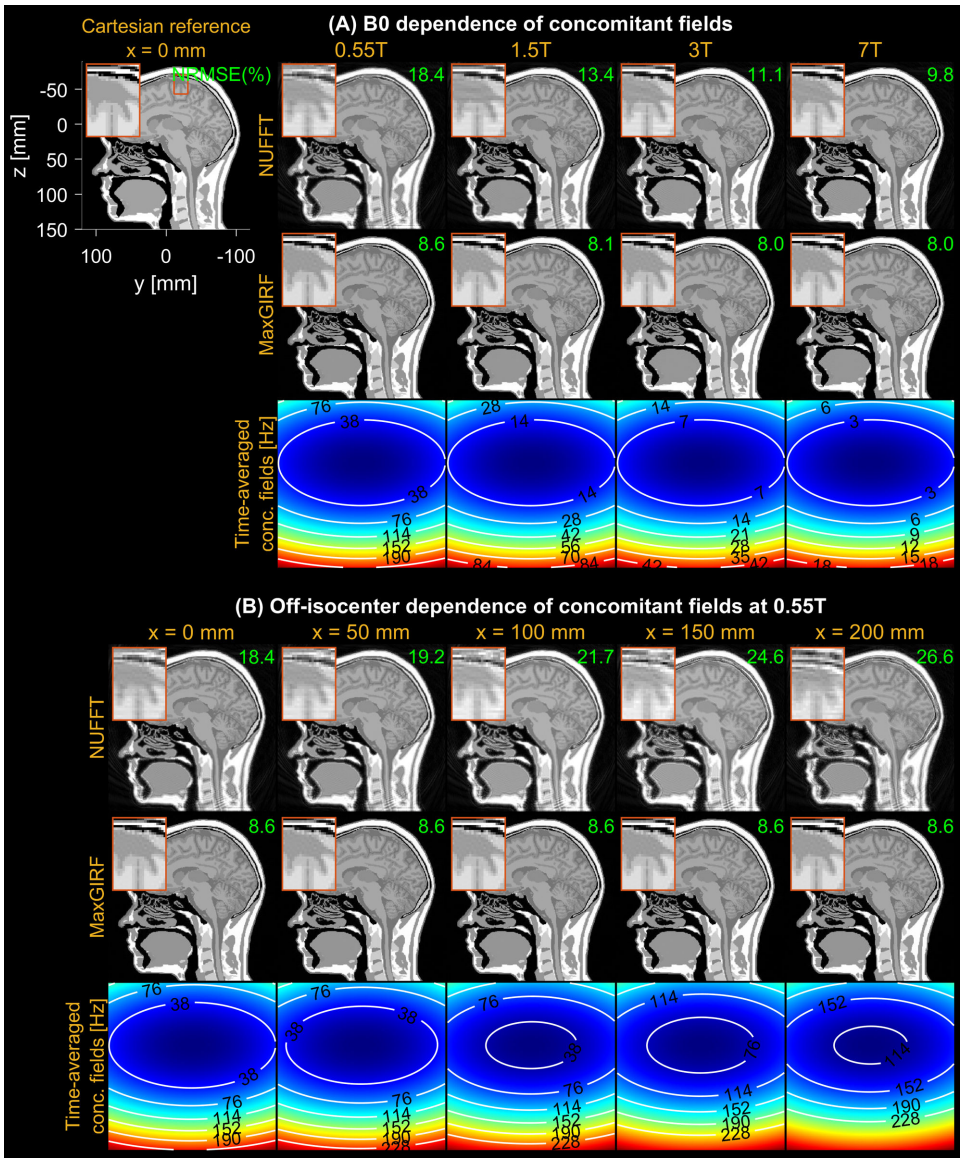

Figure 3.

Evaluation of concomitant field correction using MaxGIRF reconstruction of noiseless numerical simulations. (A) Dependence of concomitant fields on B0, using field strengths (0.55T, 1.5T, 3T, 7T) at a slice position of 0 mm from isocenter. A reference image used to simulate non-Cartesian k-space data is shown along with the physical coordinate system. The NRMSE between the ground truth and spiral reconstruction is shown (green), with 8.6% (neglecting small changes at higher field strengths) being the minimum achievable error from the difference between Cartesian and spiral image reconstructions. (B) Dependence of concomitant fields on off-isocenter distance are demonstrated for sagittal prescription. A time-averaged concomitant field map indicates the relative strength of concomitant fields at various B0 and distances from isocenter. NUFFT reconstruction shows increased spatial blurring as the field strength decreases and the distance from isocenter increases.

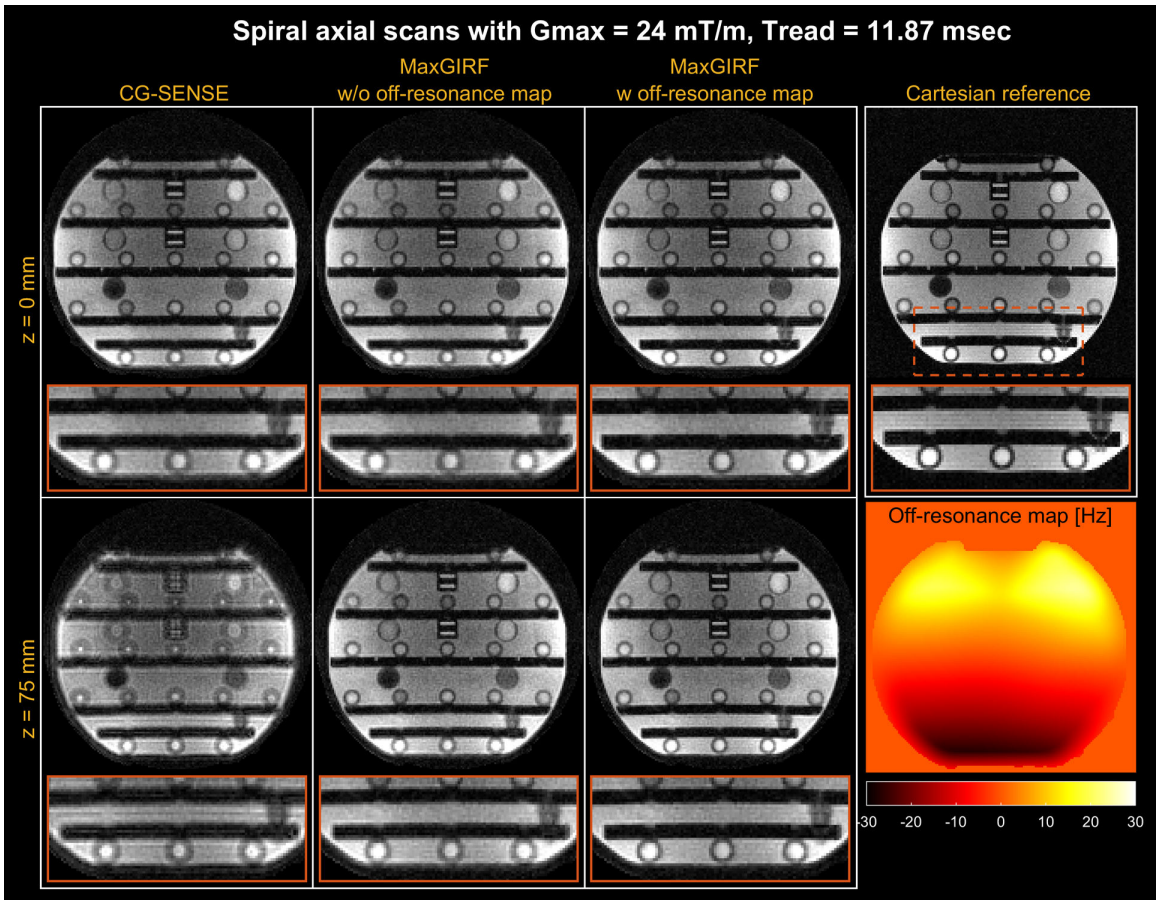

Figure 4.

Spiral axial imaging of an ISMRM/NIST phantom at 0.55T. (top row) isocenter; (bottom row) off-isocenter with z = 75 mm. A 2D Cartesian GRE reference is also shown (TE and SNR are not matched). CG-SENSE (1st column) clearly shows spatial blurring caused by both concomitant fields and static off-resonance. MaxGIRF can be applied without (2nd column) and with (3rd column) a separately acquired static off-resonance map. MaxGIRF without a static off-resonance map dramatically improves the image quality from CG-SENSE and further improvements are achieved with a static off-resonance map (one exemplary region shown in the orange box).

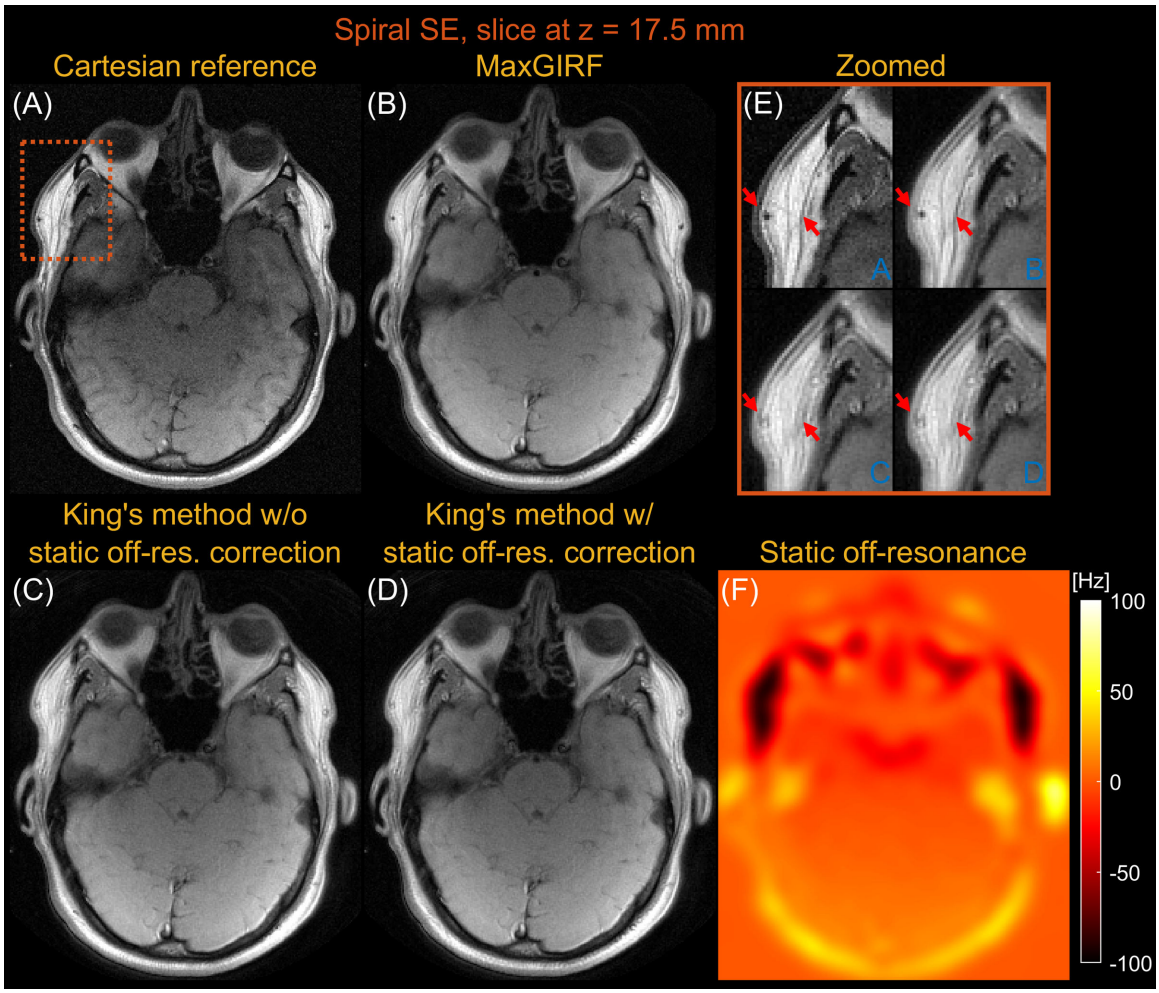

Figure 5.

Axial spiral spin-echo imaging of a healthy volunteer at 0.55T close to isocenter (z = 17.5mm). Comparison of image reconstructions using (A) comparator Cartesian spin-echo image, (B) MaxGIRF reconstruction with static off-resonance correction (Low-rank approximation L = 8), (C) King's method without static off-resonance correction, and (D) King's method with static off-resonance correction. (E) Zoomed-in image of a region with large static off-resonance (orange box). (F) Static off-resonance map. King's method with static off-resonance correction shows minor improvements compared to without static off-resonance correction in regions with strong, sharply varying static off-resonance. In contrast to both King's methods, MaxGIRF reconstruction successfully resolves local blurring due to strong off-resonance and provides features comparable to the Cartesian spin-echo image (e.g., orange box).

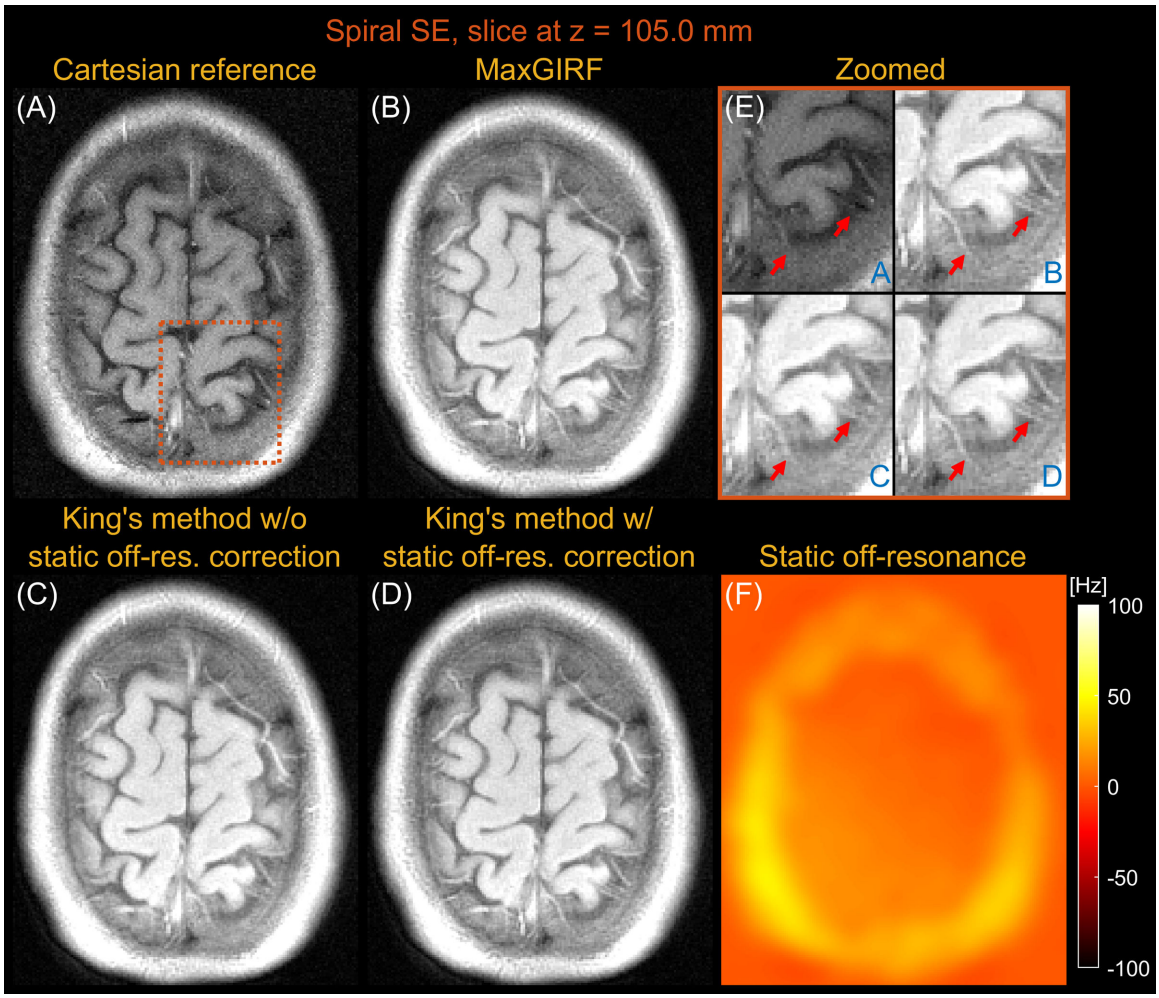

Figure 6.

Axial spiral spin-echo imaging of a healthy volunteer at 0.55T far from isocenter (z = 105.0mm). Comparison of image reconstructions using (A) comparator Cartesian spin-echo image, (B) MaxGIRF reconstruction with static off-resonance correction (Low-rank approximation L = 8), (C) King's method without static off-resonance correction, and (D) King's method with static off-resonance correction. (E) Zoomed-in image (orange box). (F) Static off-resonance map. For an axial slice without angulation, the effect of concomitant fields is merely a time-varying global frequency offset and thus all three methods successfully resolve spatial blurring due to concomitant fields when compared to NUFFT (not shown). In contrast to its performance in Figure 5, King's method with static off-resonance correction performs well particularly in this slice because a static off-resonance map varies slowly in space, which is required for successful application of most noniterative off-resonance correction methods. MaxGIRF reconstruction based on iterative CG shows improved delineation of tissue boundaries compared to King's method without static off-resonance correction, regardless of characteristics (slowly varying or sharply varying) in a static off-resonance map.

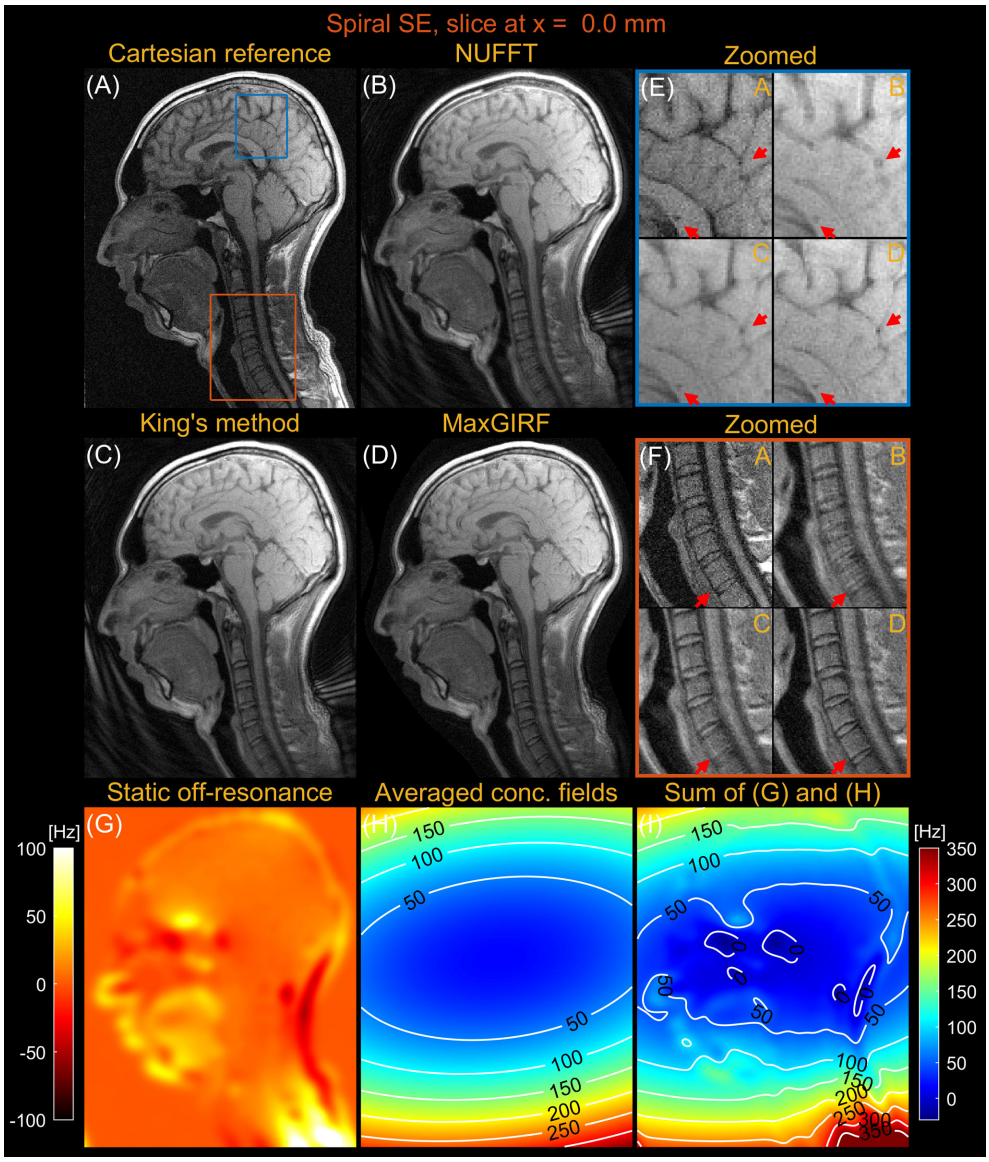

Figure 7.

Sagittal spiral spin-echo imaging of a healthy volunteer at 0.55T at isocenter (x = 0.0 mm). Comparison of image reconstructions using (A) comparator Cartesian spin-echo image, (B) NUFFT reconstruction, (C) King's method without static off-resonance correction, and (D) MaxGIRF reconstruction with static off-resonance correction (Low-rank approximation L = 30). (E) Zoomed-in image of a brain region (blue box). (F) Zoomed-in image of a neck region (orange box). (G) Static off-resonance map. (H) Time-averaged concomitant fields map. (I) Sum of the static off-resonance map and time-averaged concomitant fields map. Although MaxGIRF utilizing static off-resonance is shown in (F), MaxGIRF without static off-resonance (not shown) is of comparable quality. Thus, this indicates that the improvements in the spine region by MaxGIRF are largely attributed to the methodological difference between King's method and MaxGIRF.

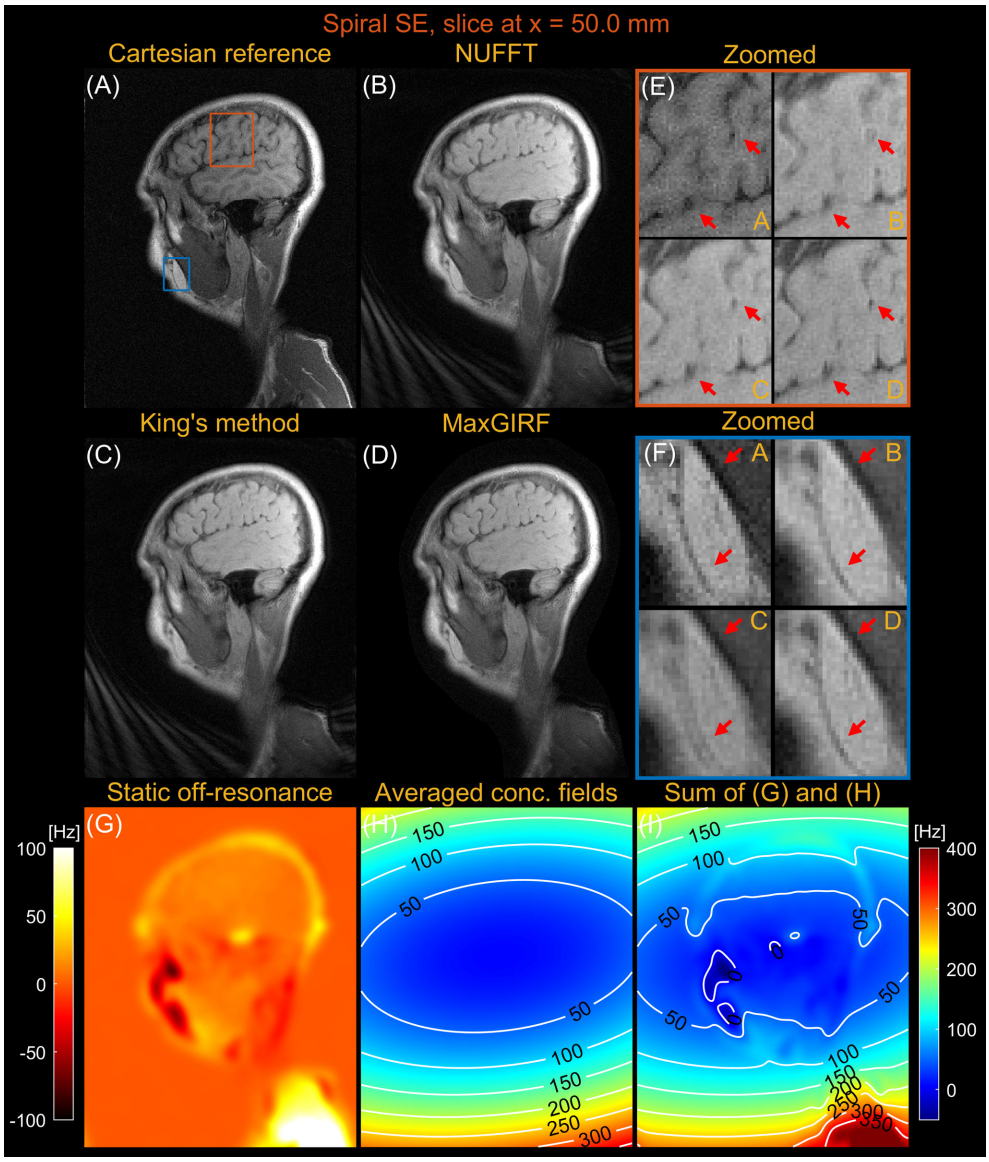

Figure 8.

Sagittal spiral spin-echo imaging of a healthy volunteer at 0.55T off-isocenter (x = 50.0 mm). Comparison of image reconstructions using (A) comparator Cartesian spin-echo image, (B) NUFFT reconstruction, (C) King's method without static off-resonance correction, and (D) MaxGIRF reconstruction with static off-resonance correction (Low-rank approximation L = 30). (E) Zoomed-in image of a brain region (orange box). (F) Zoomed-in image (blue box). (G) Static off-resonance map. (H) Time-averaged concomitant fields map. (I) Sum of the static off-resonance map and time-averaged concomitant fields map. King's method may adversely increase blurring artifacts (e.g., blue box) compared to NUFFT reconstruction when the static off-resonance in a region counteracts the concomitant fields. However, MaxGIRF with static off-resonance correction correctly handles such regions as shown in (F) and provides "sharper" delineation of brain tissue boundaries in (E) compared to King's method.

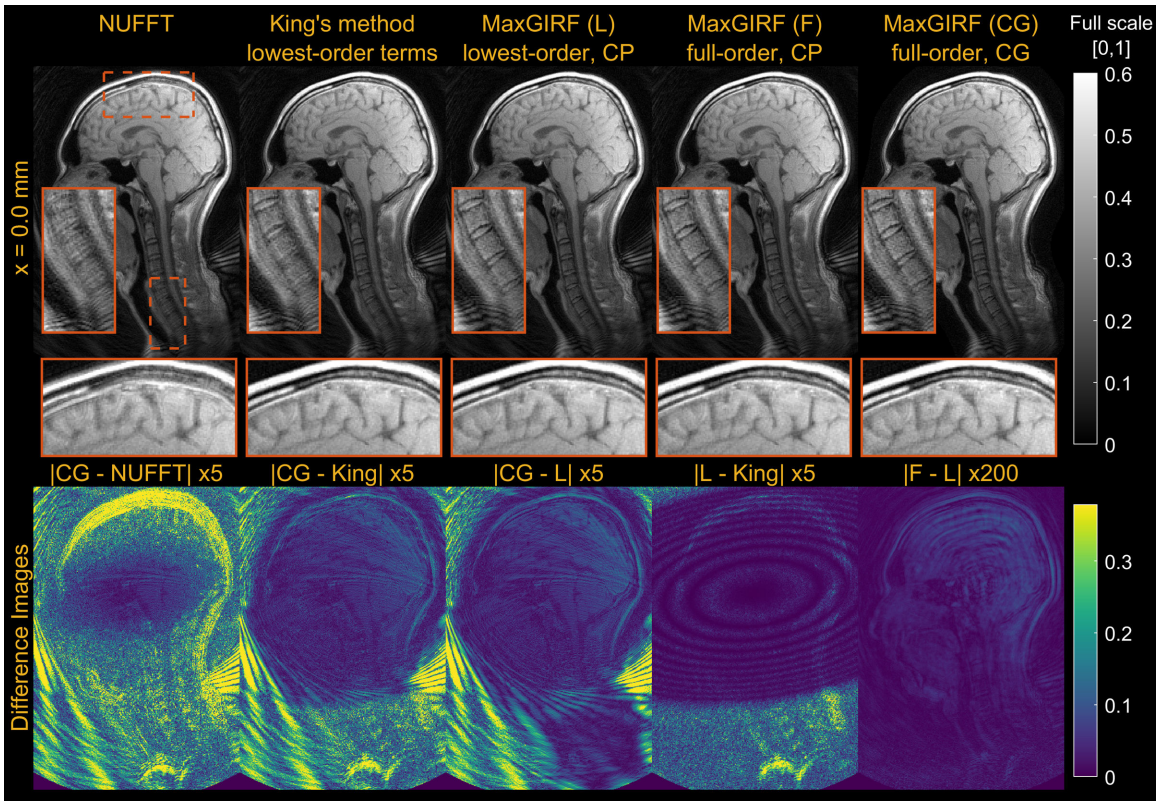

Figure 9.

Comparison of reconstruction methods compensating a different number of concomitant field terms. Mid-sagittal spiral imaging of a healthy volunteer at isocenter at 0.55T. (1st column) NUFFT. (2nd column) King's method without static off-resonance correction. (3rd column) Conjugate phase reconstruction-based MaxGIRF using only lowest-order terms in the concomitant fields. (4th column) Conjugate phase reconstruction-based MaxGIRF using entire terms in the concomitant fields (full-order). (5th column) CG-based MaxGIRF using full-order terms. (Bottom) Absolute difference images between reconstructions. GIRF-predicted gradients were used in all reconstructions. Static off-resonance correction was not performed, in order to isolate the difference due to concomitant field correction. The spiral trajectory was designed for 224 × 224 mm^2 FOV and reconstructed at twice the FOV with the same spatial resolution, which causes the aliasing at the back of the neck.

Table 1

Concomitant field basis functions $\{p_\ell(\mathbf{r})\}_{\ell=1}^{N_\ell}$ and dynamic coefficients $\{h_{\ell,i}(t)\}_{\ell=1}^{N_\ell}$ for an MR system with symmetric gradient coils and zero gradient nonlinearity.

Concomitant field basis functions	Dynamic coefficients	Type
$p_1(\mathbf{r}) = x$	$h_{1,i}(t) = G_{x,i}(t)$	gradient
$p_2(\mathbf{r}) = y$	$h_{2,i}(t) = G_{y,i}(t)$	
$p_3(\mathbf{r}) = z$	$h_{3,i}(t) = G_{z,i}(t)$	
$p_4(\mathbf{r}) = \mathrm{x}^2$	$h_{4,i}(t) = G_{z,i}^2(t)/(8B_o)$	lowest-order
$p_5(\mathbf{r}) = \mathrm{y}^2$	$h_{5,i}(t) = G_{z,i}^2(t)/(8B_o)$	
$p_6(\mathbf{r}) = \mathrm{z}^2$	$h_{6,i}(t) = \left(G_{x,i}^2(t) + G_{y,i}^2(t)\right)/(2B_o)$	
$p_7(\mathbf{r}) = xy$	$h_{7,i}(t) = 0$	
$p_8(\mathbf{r}) = yz$	$h_{8,i}(t) = -G_{y,i}(t)G_{z,i}(t)/(2B_o)$	
$p_9(\mathbf{r}) = xz$	$h_{9,i}(t) = -G_{x,i}(t)G_{z,i}(t)/(2B_o)$	
$p_{10}(\mathbf{r}) = \mathrm{x}^3$	$h_{10,i}(t) = -\left(G_{x,i}(t)G_{z,i}^2(t)\right)/\left(8B_o^2\right)$	$1/B_o^2$ order
$p_{11}(\mathbf{r}) = \mathrm{y}^3$	$h_{11,i}(t) = -\left(G_{y,i}(t)G_{z,i}^2(t)\right)/\left(8B_o^2\right)$	
$p_{12}(\mathbf{r}) = \mathrm{z}^3$	$h_{12,i}(t) = -\left(G_{z,i}(t)\left(G_{x,i}^2(t) + G_{y,i}^2(t)\right)\right)/\left(2B_o^2\right)$	
$p_{13}(\mathbf{r}) = \mathrm{x}^2 y$	$h_{13,i}(t) = -\left(G_{y,i}(t)G_{z,i}^2(t)\right)/\left(8B_o^2\right)$	
$p_{14}(\mathbf{r}) = \mathrm{x}^2 z$	$h_{14,i}(t) = -\left(G_{z,i}^3(t)/4 - G_{x,i}^2(t)G_{z,i}(t)\right)/\left(2B_o^2\right)$	
$p_{15}(\mathbf{r}) = x\mathrm{y}^2$	$h_{15,i}(t) = -\left(G_{x,i}(t)G_{z,i}^2(t)\right)/\left(8B_o^2\right)$	
$p_{16}(\mathbf{r}) = \mathrm{y}^2 z$	$h_{16,i}(t) = -\left(G_{z,i}^3(t)/4 - G_{y,i}^2(t)G_{z,i}(t)\right)/\left(2B_o^2\right)$	
$p_{17}(\mathbf{r}) = x\mathrm{z}^2$	$h_{17,i}(t) = -\left(G_{x,i}(t)\left(G_{x,i}^2(t) + G_{y,i}^2(t)\right) - G_{x,i}(t)G_{z,i}^2(t)\right)/\left(2B_o^2\right)$	
$p_{18}(\mathbf{r}) = y\mathrm{z}^2$	$h_{18,i}(t) = -\left(G_{y,i}(t)\left(G_{x,i}^2(t) + G_{y,i}^2(t)\right) - G_{y,i}(t)G_{z,i}^2(t)\right)/\left(2B_o^2\right)$	
$p_{19}(\mathbf{r}) = xyz$	$h_{19,i}(t) = \left(G_{x,i}(t)G_{y,i}(t)G_{z,i}(t)\right)/B_o^2$	